MEASUREMENT OF SEVERAL D^+ HADRONIC BRANCHING FRACTIONS WITH FINAL STATE INCLUDING K^+K^-

by

PENG ZHOU

DISSERTATION

Submitted to the Graduate School

of Wayne State University,

Detroit, Michigan

in partial fulfillment of the requirements

for the degree of

DOCTOR OF PHILOSOPHY

2012

MAJOR: PHYSICS

Approved by:

_____

Advisor   Date

_____

_____

_____

To my family and my advisor

ACKNOWLEDGMENTS

TABLE OF CONTENTS

LIST OF TABLES

LIST OF FIGURES

Chapter 1:   Introduction

1.1   Standard Model

The Standard Model of particles is a theory that describes elementary particles and describes the electromagnetic, weak and strong interaction between those particles. The structure of the Standard Model was developed in the mid to late 20th century. Chronologically, in the 1960s there was the formulation of quark mixing [1] and of an electroweak $SU(2) \times U(1)$ model with four quarks, four leptons, and all the weak bosons described in Section 1.2 [2] [3] [4] in 1967 and 1968. In the 1970s, QCD was formulated as a $SU(3)$ theory [5, 6], and in the 1970s and 1980s three generations of fundamental fermions were incorporated into the model through CP-violating mixing [7], discovery of the τ lepton and b quark. The Model was completed in the 1990s with first observations of the top quark and tau neutrino, and observation of CP-violating effects in mesons containing a b quark.

1.2   Fundamental particles

Fundamental particles have no substructure, and are described as point-like. They are the basic building blocks of all other particles. In the Standard Model, fundamental particles are arranged in two big groups (based on the spin of particle). Fundamental fermions, having spin 1/2, include quarks, leptons and their antiparticles. Fundamental bosons, having integer spin, which include gauge bosons and Higgs bosons, Fig. 1.1.

Three Generations of Matter (Fermions)

	I	II	III	
mass→	2.4 MeV/c²	1.27 GeV/c²	171.2 GeV/c²	0
charge→	⅔	⅔	⅔	0
spin→	½ u	½ c	½ t	1 γ
name→	up	charm	top	photon
	4.8 MeV/c²	104 MeV/c²	4.2 GeV/c²	0
	-⅓ d	-⅓ s	-⅓ b	0 g
	½	½	½	1
	down	strange	bottom	gluon
	<2.2 eV/c²	<0.17 MeV/c²	<15.5 MeV/c²	91.2 GeV/c²
	0 νₑ	0 ν_μ	0 ν_τ	0 Z⁰
	½	½	½	1
	electron neutrino	muon neutrino	tau neutrino	Z boson
	0.511 MeV/c²	105.7 MeV/c²	1.777 GeV/c²	80.4 GeV/c²
	-1 e	-1 μ	-1 τ	±1 W±
	½	½	½	1
	electron	muon	tau	W boson

Quarks — Leptons — Gauge Bosons

Figure 1.1:   Standard Model of Elementary Particles.

1.2.1   Fundamental bosons

There are two fundamental bosons, gauge bosons and Higgs bosons. The gauge bosons in the Standard Model are photons, which carry electromagnetic interaction, W and Z bosons which carry the weak interaction and gluons which carry the strong interaction. They all have spin 1.

The Higgs boson has spin zero. It must be present or the Model will give infinite results for some scattering amplitudes, such as $W - W$ scattering at large energy. Experimental searches for the Higgs bosons are still ongoing.

1.2.2   Fundamental fermions

Fundamental fermions in the Standard Model include quarks and leptons. All particles have anti-particle partners, with the same mass and opposite charge.

Quarks form the vast majority of subatomic particles, called hadrons, which interact strongly with other hadrons. Quarks carry a quantum number called color, which can exist in three types, conventionally named red, green and blue. Only states with zero color can be stable or meta-stable with respect to the strong interaction. Free quarks can not be observed, because the potential energy obtained by separating the quarks in a hadron by macroscopic distances is much larger than the quark rest energy $m_q c^2$. New quarks and antiquarks will be generated along the field lines and they will recombine with the original quarks.

Quarks have various intrinsic properties, including charge, color, and mass. Table 1.1 shows some properties of all quarks. Their charge is a fraction of the charge of the electron, either -1/3 or +2/3 for quarks.

From Fig. 1.1 there are in total 6 different quarks and they are split into 3 different generations. First generation have up and down quarks (u and d) which have lowest masses of all quarks. Second generation have charm and strange quarks (c and s) and third generation has top and bottom (t and b) quarks. Quarks change from those of the first row to those of the second row or viceversa by emitting or absorbing a $W^{\pm}$, Fig. 1.2. The up and down quarks are lighter and therefore more stable than other heavier quarks and those heavier quarks would decay to up and down quarks through repeated particle decays.

Stable hadrons can be formed in two ways: first, by combining a quark (say, red) with an anti-quark (say, anti-red). There is no net color, and the particles obtained this way are called mesons and have integer spin. Kaons and pions are, for example, mesons with wavefunction indicated as $|u\bar{s}>$ and $|d\bar{u}>$ respectively (this representation of the wavefunction indicates quark content). Second, three quarks (red, green and blue) can be combined to form a baryon, with half-integer spin. Combination of three anti-quarks will produce an antibaryon. The proton is an example of baryon and is indicated as $|uud>$.

Family	Name	Charge	Mass	Spin
I	u	$+\frac{2}{3}$	1-4 MeV	1/2
	d	$-\frac{1}{3}$	4-8 MeV	1/2
II	c	$+\frac{2}{3}$	1.15-1.35GeV	1/2
	s	$-\frac{1}{3}$	$80 - 130 MeV$	1/2
III	t	$+\frac{2}{3}$	174GeV	1/2
	b	$-\frac{1}{3}$	$4.1 - 4.4 GeV$	1/2

Table 1.1: Quarks in the Standard Model

Leptons could also be separated into three generations, just as quarks, first are electron, neutrino and anti-particles, second are muon, related neutrino and third are tau. Properties of these leptons are shown in Table 1.2. Unlike quarks, lepton interact only through the electro-weak force. Fig. 1.2 shows a transition from charged lepton to neutrino through the echange of a W boson.
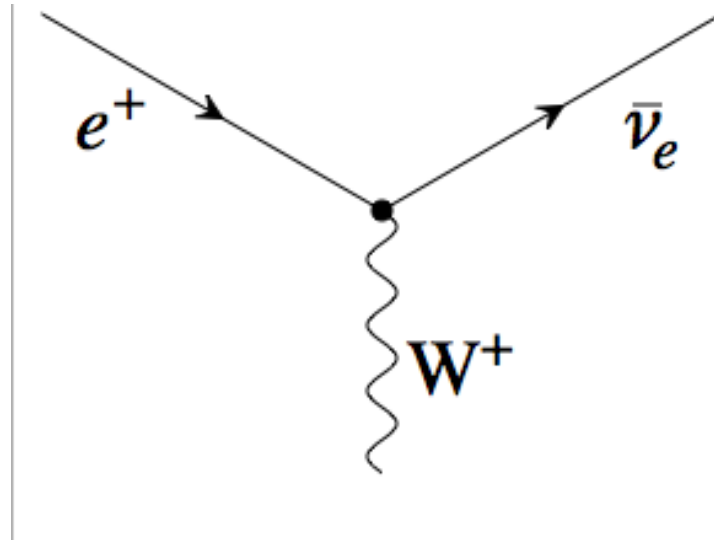
Figure 1.2: Electron neutrino interaction vertex.

In the Standard Model, the total number of quarks and the total number of leptons in a process must be conserved. However, due to mixing, the number of quarks or leptons in a given generation can not be conserved separately.

Family	Name	Charge	Mass
I	e	-1	0.511MeV
	ν_e	0	< 2eV
II	μ	-1	106MeV
	ν_μ	0	< 0.19MeV
III	τ	-1	1.78GeV
	ν_τ	0	< 18.2MeV

Table 1.2:   Leptons in the Standard Model

1.2.3   Elementary interactions

There are four different basic interactions between those fundamental particles, electromagnetic, strong, weak and gravitational interaction. Gravity is the weakest one and is not part of the Standard Model.
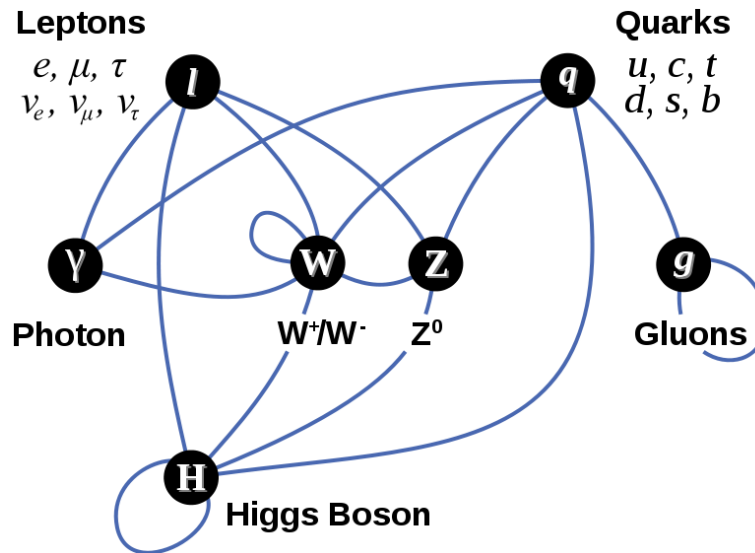
Figure 1.3:   Summary of basic interactions between particles in Standard Model.

Fig. 1.3 shows the summary of the other three interaction (no gravitational force) between those fundamental particles in Standard Model together with the exchange of gauge bosons in each interaction. Some details of interaction is also listed in table.1.3.

Electromagnetism (EM) is described classically (macroscopically) by Maxwell equations, and microscopically by Quantum Electrodynamics. Quantum Electrodynamics (QED) describes the photon, which is massless, as the mediator of EM field.

Force	Name	Charge	Mass
EM	photon(γ)	0	0
Weak	$W^{\pm}$	± 1	80.40GeV
	Z^0	0	91.188
Strong	gluon(g)	0	0

Table 1.3: Gauge bosons in the Standard Model

It is also well accepted that since the mediate particle of EM field is massless, the electromagnetic field would have infinite range.

The weak interaction is responsible for the radioactive decay of subatomic particles. It is called weak because at low energy its field strength is typically several orders of magnitude less than both the electromagnetic and strong force. The weak force was first formulated in the 1920s (by Fermi) in nuclear physics by means of a point-like vector interaction and it affects all known fermions. As shown in table 1.3, in the Standard Model, modern understanding of the weak interaction includes three crucial modifications compared to the original formulation:

- the fermions involved in the interaction are left-handed. For example, virtually all interacting neutrinos will have their spin anti-aligned with respect to their direction of motion.

- it is now understood that the weak interaction proceeds by exchanging W and Z bosons, also called as charged and neutral currents.

- Since the W and Z bosons have relatively high mass (comparing to other gauge particles), the weak interaction has a very short range (but a coupling strength similar to that of the electromagnetic interaction).

The strong interaction, about 100 times stronger than the electromagnetic force, is described by Quantum Chromodynamics (QCD). QCD is a non-Abelian gauge theory based on a local symmetry group SU(3) and is mediated by gluons. From the theory, quarks and gluons are the only particles that carry color charge, and so participate

Symmetry Class	Symmetry Invariance	Conserved Quantity
Continuous Symmetry	translation in time	energy
	translation in space	Momentum
	rotation in space	Angular Momentum
Discrete Symmetry	charge conjugation (C)	charge parity
	coordinate inversion (P)	spatial parity
	time reversal (T)	time parity

Table 1.4: Some of the relations between Lagrangian symmetry and conserved physical quantity.

in the strong interaction. The strong interaction binds nuclei together and all the stable states must be colorless. Another peculiar property of QCD is Asymptotic freedom [5] [6]. The effective strength of the strong interaction decreases at short distances.

1.3   Symmetries in Physics

Symmetry is important because it is related to conservation laws in physics [8]. Emmy Noether stated that any symmetry in the Lagrangian describing a physical system has a corresponding conservation law. Each continuous symmetry of a system implies that some physical property of that system is conserved. The table 1.4 includes some fundamental symmetries and corresponding conservation laws.

For parity invariance, the process would not change when one or three spatial axes are reversed (such as when a process is observed through a mirror). Parity has only two possible values (-1 or +1), which are called odd and even parity. To the best of our knowledge, parity is conserved in electromagnetic and strong interaction but not in the weak interactions, where it turns out to be maximally violated [9] [10].

The weak interaction also violates charge invariance, but the charge-parity symmetry is conserved in the bulk of weak interactions. Our current model of fundamental interaction is based on CPT conservation, that is, all phenomena are invariant if spatial axes are reversed, the time arrow is reversed, and charges are reversed.

1.4 Cabibbo-Kobayashi-Maskawa matrix

Nicola Cabibbo [1] studied the phenomena that the transitions with change in strangeness had amplitudes only one fourth of those with no change in strangeness. He solved this issue by implying a factor mixing angle θ_C (also called Cabibbo angle). Cabibbo stated that the weak coupling of quarks should be exactly as strong as the weak coupling of electrons and neutrinos. However, different quarks (different mass eigenstates), mix, and the larger mixing is between s and d quarks (or equivalently, to high precision, between u and c quarks). That largest mixing is the "Cabibbo angle", which is measured to be about 13.1° [11]. Interactions with amplitude proportional to $\cos\theta_C$ are Cabibbo favored, while interactions with amplitude proportional to $\sin\theta_C$ are Cabibbo suppressed.

At the time of Cabibbo's paper, only three quarks (u, d, s) were known. But the theory failed to explain the amplitude of the decay $K^0 \to \mu^+\mu^-$. Based on that theory, this amplitude was predicted to have the same strength as the commonly observed purely leptonic decays of the K^-, with an additional factor $\sin\theta_C\cos\theta_C$. But the actual branching fraction is less than 10^{-7}. The idea that there exists a fourth quark, which would create a symmetrical quark and lepton sector, was further studied by Glashow [12]. The fourth quark would then cancel the amplitude of this decay.

The adding of the fourth quark (actually named charm) suggests that weak interactions with quarks can be portrayed as a rotation of s and d quarks. And it could be expressed as

$$\begin{pmatrix} d' \\ s' \end{pmatrix} = \begin{pmatrix} V_{ud} & V_{us} \\ V_{cd} & V_{cs} \end{pmatrix} \begin{pmatrix} d \\ s \end{pmatrix} \tag{1.1}$$

or in terms of the Cabibbo angle:

$$\begin{pmatrix} d' \\ s' \end{pmatrix} = \begin{pmatrix} \cos\theta_C & \sin\theta_C \\ -\sin\theta_C & \cos\theta_C \end{pmatrix} \begin{pmatrix} d \\ s \end{pmatrix} \tag{1.2}$$

where d' and s' are weak eigenstates, a mixture of mass states d and s. This 2×2 rotation matrix V_{ij} is called the Cabibbo matrix and $|V_{ij}|^2$ is proportional to the probability that quark of flavor i decays into a quark of flavor j (except for phase space factors).

The observation of CP-violation could not be explained by a four quark model. Kobayashi and Maskawa expanded the Cabibbo matrix [13] to include a third generation, top and bottom quarks. The new 3×3 matrix is called Cabibbo-Kobayashi-Maskawa matrix (CKM matrix):

$$\begin{pmatrix} d' \\ s' \\ b' \end{pmatrix} = \begin{pmatrix} V_{ud} & V_{us} & V_{ub} \\ V_{cd} & V_{cs} & V_{cb} \\ V_{td} & V_{ts} & V_{tb} \end{pmatrix} \begin{pmatrix} d \\ s \\ b \end{pmatrix} \tag{1.3}$$

The CKM matrix describes the probability of a transition from one quark i to another quark j and the transitions are proportional to $|V_{ij}|^2$. Kobayashi and Maskawa used three angles and one phase to describe the parameter V_{ij}.

$$V = \begin{pmatrix} c_1 & s_1 c_3 & s_1 s_3 \\ -s_1 c_2 & c_1 c_2 c_3 - s_2 s_3 e^{i\delta} & c_1 c_2 s_3 + s_2 c_3 e^{i\delta} \\ -s_1 s_2 & c_1 s_2 c_3 + c_2 s_3 e^{i\delta} & c_1 s_2 s_3 - c_2 c_3 e^{i\delta} \end{pmatrix} \tag{1.4}$$

In the equation, c_i and s_i are the cosines and sines of the three angles and δ is the CP-violating phase. Currently, the experimental value of CKM matrix elements [11] is

$$
V \simeq \begin{pmatrix}
0.97428 \pm 0.00015 & 0.2253 \pm 0.0007 & 0.00347^{+0.00016}_{-0.00012} \\
0.2252 \pm 0.0007 & 0.97345^{+0.00015}_{-0.00016} & 0.0410^{+0.0011}_{-0.0007} \\
0.00862^{+0.00026}_{-0.00020} & 0.0403^{+0.0011}_{-0.0007} & 0.999152^{+0.000030}_{-0.000045}
\end{pmatrix} . \qquad (1.5)
$$

1.5 D mesons and hadronic decays

The charm quark was first discovered in 1974 at the Stanford Linear Accelerator Center and the Brookhaven National Laboratory [14] [15]. They both discovered a new heavy particle (mass about 3.1GeV) with much longer lifetime than those with similar mass. This new particle was interpreted as a state of charm and anti-charm quark ($|c\bar{c}>$) and named $J\psi$.

D (D^+, D_s or D^0) mesons are the lightest mesons containing a singe charm quark, and the D^+, discussed in this analysis, has a wave function with charm and anti-down quarks ($|c\bar{d}>$). D mesons also have the same parity and angular momentum as pions and kaons ($J^P = 0^-$). D mesons live for about 1 ps before they decay weakly. Fig. 1.4 [16] shows several typical charm decays.
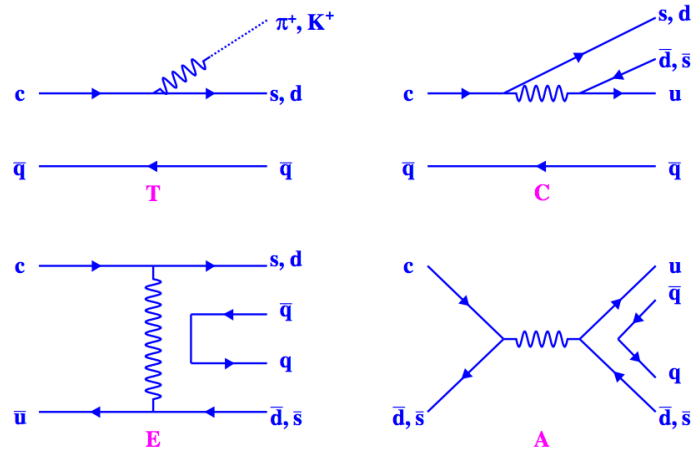
Figure 1.4:   typical quark flow diagram indicating charm decays. T: color-favored decay; E: exchange; C: Color-suppressed decay; A: annihilation.

The study of Cabibbo suppressed hadronic decays of the charm hadrons can pro-

vide valuable information about the underlying QCD matrix elements [17], for example, relates the amplitudes associated to Cabibbo suppressed quasi-two-body decays to measured branching ratios [18] relates Cabibbo suppressed branching ratios to various models of W hadronization. It is noted that some of the decays studied below, such as $D^+ \to \phi\rho^+$ are necessarily color suppressed.

The motivation for completing this analysis, however, was mostly to drastically improve some current branching ratios measurements listed in Table 1.5, where charge conjugate modes are also implied. First, the top three branching ratios are measured with a precision one order of magnitude below that of the other ones. Second, a comparison of current data shows the ratio

$$ R = \frac{B(D^+ \to \phi\pi^+\pi^0) + B(D^+ \to \phi\pi^+)}{B(D^+ \to \phi X)} = 2.8 \pm 1.0 \tag{1.6} $$

significantly exceeds the upper limit of one. Third, the decay $D^+ \to \phi\rho^+$ has long been predicted [17] and has been searched for, as seen in Table 1.5, but has never been observed before.

Table 1.5: Summary of $D^+ \to K^+K^-X$ branching ratios [11].

Decay mode	Branching ratio (%)
$D^+ \to K^+K^-\pi^+\pi^0$, non ϕ	1.5 ± 0.7
$D^+ \to \phi\pi^+\pi^0$	2.3 ± 1.0
$D^+ \to K^+K^-\pi^+\pi^0$	2.7 ± 1.2
$D^+ \to \phi\rho^+$	< 1.5 (90% C.L.)
$D^+ \to \phi\pi^+$	0.542 ± 0.018
$D^+ \to \phi\pi^+ + D^+ \to \phi\pi^+\pi^0$	2.84 ± 1.02
$D^+ \to \phi X$	1.03 ± 0.12
$D^+ \to K^+K^-\pi^+\pi^+\pi^-$	0.0022 ± 0.0012
$D^+ \to K^+K^-K^+$	0.00087 ± 0.00020

The decay amplitudes for the D decay to two vector states, $D(q) \to V_1(q_1)V_2(q_2)$ can be written as [17]:

$$M(D(q) \to V_1(q_1, \lambda_1)V_2(q_2, \lambda_2)) =$$
$$\frac{-i(2\pi)^4\delta^4(q - q_1 - q_2)}{\sqrt{8V^3 q_0 q_{10} q_{20}}}(iC\delta_{\alpha\beta} + iD\epsilon_{\mu\alpha\nu\beta}q_{1\mu}q_{2\nu} + iEq_{1\beta}q_{2\alpha})\epsilon_\alpha^{(\lambda_1)}(q_1)\epsilon_\beta^{(\lambda^2)}(q_2)$$

$$(1.7)$$

where the q_i refer to the four momentum of particle i and the λ_i account for the spin of the two vector particles.

In the equation, C, D and E are constants representing the invariant amplitudes, C is in $10^6 GeV^{-1}$ while D and E are in $10^6 GeV$. The value of these amplitudes are obtained by fitting the branching ratios of better measured related branching fractions, such as $D \to K^* \rho$. From Ref. [17], the expected branching ratio for $D^+ \to \phi\rho^+$ from the calculation is 1.2×10^{-3}. It will be seen in Chapter 4 that our result is substantially higher.

In Chapter 2 we will present CLEO experiment for the analysis. Chapter 3 and 4 will presents the detail of experiment method and the results of this analysis.

Chapter 2:   The CLEO-c Experiment

Accelerators and detectors are the basic building blocks of experimental high energy physics. Accelerators provide a combination of particle fluxes and energies much higher than those found in nature.

CLEO-c is a dedicated program of charm physics at the Cornell Electron Storage Ring, which is also called CESR, with the goal of elucidating weak and strong physics behind charm and bottom quark decays. The entire system of CLEO-c and CESR is optimized for electron-positron annihilation at energies of 3 to 5 GeV. For 20 years before, CLEO in various editions and CESR worked at energies of about 10 GeV.

For the analysis described here, the data were collected at a total beam energy of 3.770 GeV. That is the energy corresponding to the mass of the third known charmonium resonance, which is also the first for which strong decays become dominant (a fact evidenced by its several MeV width). The resonance decays predominantly into

$$e^+ e^- \rightarrow \psi(3770) \rightarrow D\bar{D} \tag{2.1}$$

where $D = (D^+, D^0)$. The combination of abundant particle yield and exclusive two-particle decay enables a lot of precision measurements.

There are or were several other experiments doing similar measurements, such as BES and, in the past, Mark III, as well as fixed target experiments such as FOCUS. But CLEO-c are unique because of several reasons [19]:

1. CLEO-c has a larger data set sample (CLEO-c data sample are about 200-500 times larger than Mark III).

2. Those produced charm events at threshold are very clean and at the same time,

these charm events are pure $D\bar{D}$ with no additional fragmentation particles produced.

3. The complete reconstruction of one D allows the very clean study of the other particle in the event, nearly eliminating combinatorial backgrounds.

There are other advantages by CLEO-c experiments, such as clean neutrino reconstruction in semileptonic decays, by reconstructing all particles in the event except the neutrino and applying kinematic constraints, but these 3 factors are the most important in this analysis.

2.1 The Cornell Electron Storage Ring (CESR)

The CESR [20], is 768 meter long, buried 40 feet beneath Alumni Field on Cornell University campus area in Ithaca, NY. CESR was completed in 1979 and was to store beams accelerated by the Cornell Synchrotron (an earlier machine used for fixed target experiments), is an electron-positron collider operating at a center-of-mass energy in the range of 3.0 to 12 GeV.

There are 3 major parts in CESR, As shown in Fig. 2.1, they are linear accelerator (linac), synchrotron, and the storage ring. The CESR storage ring is housed in the same circular tunnel as the synchrotron, as shown in Fig. 2.2. The CLEO-c Detector, where data from electron-positron interaction are collected, are located at the bottom (in the South end) of Fig. 2.1. The area is also known as the Interaction Region, while the small volume where collisions take place (about 20 mm in length along the beam pipe, with a height of $10\mu m$ and a horizontal width of about 1mm) is called the Interaction Point (IP).
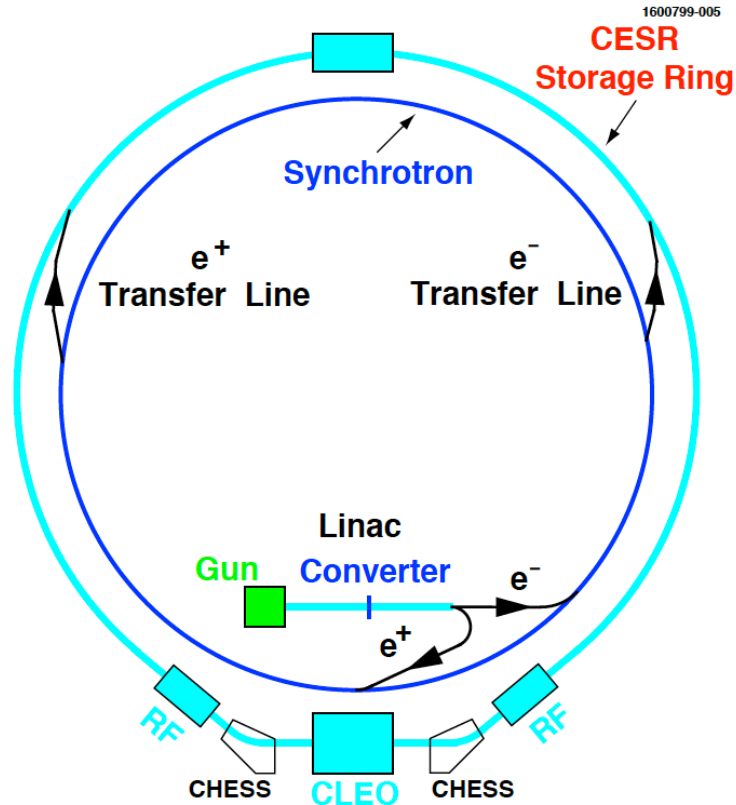
Figure 2.1: Structure of Cornell Electron Storage Ring

2.1.1 Linear Accelerator and synchrotron in CESR

In the linear accelerator, electrons are created at the beginning from a 150 keV electron-gun, while positrons are created by diverting accelerated electrons to bombard a tungsten target. The collision generates photons, which then undergo pair production in matter to create electron-positron pairs. Finally the created positrons are collected and accelerated in the Linear Accelerator, which accelerates alternatively electrons and positrons before they are injected into synchrotron. In the synchrotron they accelerate further, and due to the charge, positron will travel clockwise in the synchrotron. Electrons, always injected later than positrons, travel counter-clockwise in the synchrotron.

Figure 2.2: Picture taken in the tunnel, with synchrotron on the left and storage ring on the right

2.1.2 Storage Ring in CESR

Electrons and positrons are injected into the Storage Ring after they reach the expected energy and, under the effect of RF cavities, form small bunches. CESR is able to operate with a maximum of 45 bunches, and the time difference between adjacent bunches is about 14 ns.

Because there are many bunches with only a single ring, there will be multiple crossing points. Only one is wanted, the one where the beams collide in the center of the CLEO-c detector, which is called the Interaction Point, or IP. Generally, the beams interact with one another and the beam-beam interaction is the largest source of beam instability and lifetime. There are twice as many crossing points as there are bunches, or up to 90 crossing points. To avoid this, electron and positron beams are kept in "pretzel orbits", where the beams move about in the transverse plane under the influence of electrostatic deflectors so as to be well separated from the opposing beam at all the crossing points except the IP. Due to the pretzel scheme, when electron and positron beams reach the IP, they have a very small crossing angle, about 2.5 mrads.

2.1.3 Other Technical systems

The CESR beams have lifetimes of order one hour, and they must travel in high vacuum to minimize scatter and loss of beam particles. The vacuum enclosure is a long thin toroid called the Beam Pipe, with diameter of about 12 cm at most places in the storage ring, and 2.5 cm at the IP. Near CLEO, the vacuum is produced by Titanium Sublimation Pumps (TiSPs) and the beam pipe pressure is less than 1.33×10^{-7} Pa.

The Radio Frequency (RF) Accelerating System restores the energy lost by the beam particles in synchrotron radiation. Currently, the CESR RF system has four superconducting cavities, which provide accelerating gradient at about 6.2 MV/m to high current 5.3 GeV beams. Also four klystrons are available to provide power to these cavities. At the same time, dipole magnets are used in the synchrotron to maintain the circular orbit of electrons and positrons. The field of these dipole magnets must ramp up at injection to keep the orbit stable while both beams are accelerating. In CESR, there are 192 dipole magnets. The storage ring also has 92 quadrupole magnets to focus the beam to to its nominal orbit.

2.1.4 Luminosity and Upgrade of CESR

Luminosity is the most important parameter in judging the performance of the storage ring since it is proportional to the number of recorded events. The CESR luminosity has been continuously improving since CLEO started taking data in 1980.

Luminosity (L) is used in the equation $R = L\sigma$, where R is the instantaneous event rate (units of Hertz), and σ the relativistically invariant cross section for the process of interest (units of area). Since σ is determined by Nature, the only way to improve the event rate is to improve L. For collinear, equal, 3-D Gaussian beams, L is

$$L = f \frac{n_1 n_2}{4\pi \sigma_x \sigma_y}, \tag{2.2}$$

where f is the collision frequency, the n_i are the beam populations, and $\sigma_{x,y}$ are the transverse dimensions of the beams.

The total luminosity is related to the number of created events, N by

$$N = \int R(t)dt = \sigma \int L(t)dt.$$

2.2 CLEO-c overview.

There were several upgrades for CLEO detector since it was first commissioned almost 33 years ago (1979). The edition prior to CLEO-c, the CLEO III detector, was commissioned in 1999. The current upgrade only kept the electromagnetic calorimeter from CLEO III. The rest of the detector was optimized to account for the lower momenta and energies at CLEO-c, compared to CLEO III.

One of the major modifications was that the silicon vertex detector (SVD) was replaced. This is the first detector encountered by particles from the IP, and is used to measure the detached vertices of weakly decaying particles, while helping with measuring the tracks momenta.

Unfortunately, it also included substantial amounts of material in the silicon chips themselves and in the rigid carbon fiber support structure, which scatters charged particles and converts photons. At CLEO-c, charm particles are produced nearly at rest and their detached vertices are almost unobservable. So it was replaced with a lighter inner drift chamber.

The central tracker is the core of CLEO-c and any other related detector. The performance of the tracking system is quantified in terms of momentum, angle and impact parameter resolution. The CLEO-c tracking is extremely well understood,

with systematics in tracking efficiency reduced to about 0.3%.

Particle identification requires the measurement of two out of four quantities E, p, m, v. The momentum is always measured precisely by the central tracker. Two measurements for each single track exist in CLEO-c which depend on the particle velocity. The first is the particle's specific ionization (dE/dx), and the second is the Cherenkov Ring Imaging.

The CsI calorimeter is used for detecting electromagnetic showers, with close to 4π solid angle coverage around the IP.

The CLEO-c magnetic field is produced by a superconducting solenoid, placed directly behind the electromagnetic calorimeter, and aligned with the beam pipe. The field is 1.0 Tesla. Charged particles will describe helical trajectories in such a field.

The unit system used in the following is based on natural units, $c = \hbar = 1$, the unit system preferred in high energy physics so particle mass, energy and momentum have all similar scales, expressed in GeV or MeV. Also, by convention the beam pipe is along the $z-$axis, or at $|\cos\theta| = 1$.
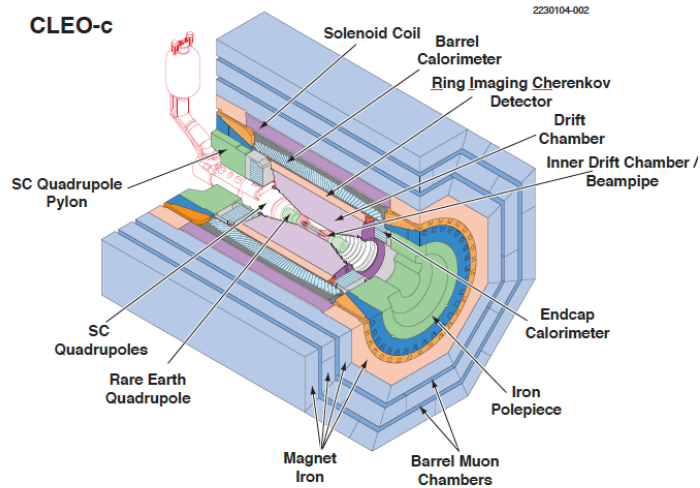
Figure 2.3: Structure of the CLEO-c detector.

2.2.1 Drift Chamber

The purpose of the drift chamber is to measure charged particle momentum vectors at the vertex and to assist in particle identification.

There are two parts of the drift chamber in the CLEO-c detector system, the Inner Drift Chamber (replacement for previous vertex chamber) and Main (Outer) Drift Chamber. The main drift chamber is a wire chamber with inner radius 12 cm and outer radius 82 cm to the beam pipe axis. It consists of 47 sense wire layers, the first 16 axial (parallel to the beam pipe) and the remaining layers grouped into 4 layers each, axial and stereo in alternance. Each layer consists of cells, with one wire at the center (sense wire, where electrons are collected), and four wires at the corner of a square, called field wires, which shape the electric field of the cell.

Charged tracks pass through these chambers and then ionize the gas in the chamber (the gas in the chamber is a 60/40 He/C_3H_8 mixture). The ionization is collected by wires which are at high voltage relative to the surrounding "field" wires. The electrical signals from the sense wires are amplified and digitized and recorded while data are taken. A charged track will be reconstructed when it hits both drift chambers. Then the momenta of reconstructed tracks are measured based on the radius of curvature and known magnetic field. The momentum resolution is about 3.5 MeV and the position resolution is about 85 μm at the IP, when the track momentum is 1 GeV.

The other important piece of information is the dE/dx, which is the energy loss per centimeter for each track and is the main information used to identify the mass of charged tracks, at least at CLEO-c energies. The dE/dx is measured in the drift chamber. The measurement will then be compared to the theoretical or expected value for the measured momentum so that a mass probability can be assigned.

The deviation from single measurement variable is defined as

$$\chi_i^2 = (\frac{dE/dx_{meas} - dE/dx_{exp}}{\sigma_i})^2 \qquad (2.3)$$

In the equation, σ_i is the uncertainty of the measurement, generally around 6%. χ_i^2 is defined for each particle hypothesis of electron, pion, kaon by summing the χ_i^2 over many hits.

The CLEO-c dE/dx resolution is illustrated by plotting the particle dE/dx vs particle momentum, shown in Fig. 2.4. The energy (dE) calibration involves both an electronic and an empirical gain calibration, and for the dx calibration, there is a large correction due to $\sin\theta$ and also a correction from the geometric path length in the $r-\phi$ projection of the drift cell. The last step is an additional dE calibration to account for gas-gain saturation, gas pressure and other effects [19].
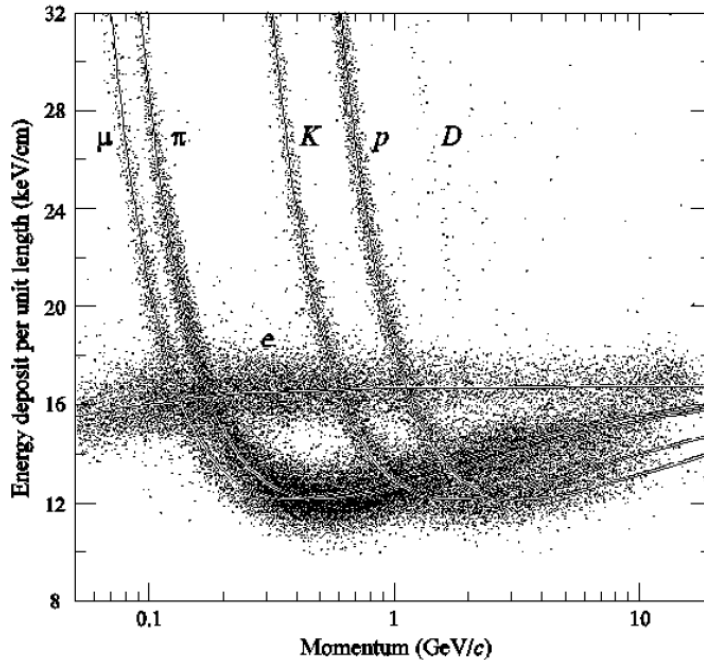
Figure 2.4: dE/dx scatter plot respect to track momentum with π K and p and μ bands.

Because kaon and pion are the main charged particle species in CLEO-c, separation between the kaon and pion hypothesis is the main figure of merit of the technique, as shown in Fig. 2.5. The separation between kaons and pions from dE/dx information depends on the momentum. When the momentum is lower than 600 MeV, the separation is greater than 5σ, and the separation will reduce to about only 1σ when

the momentum reaches about 1 GeV.

The momenta of charged particles in CLEO-c will be mostly below 1 GeV so dE/dx alone is good enough to separate kaon and pions, but some other information is needed to separate kaons and pions when the momentum is high. This motivates the use of a Cherenkov radiation detector to help in particle identification for high momentum tracks.
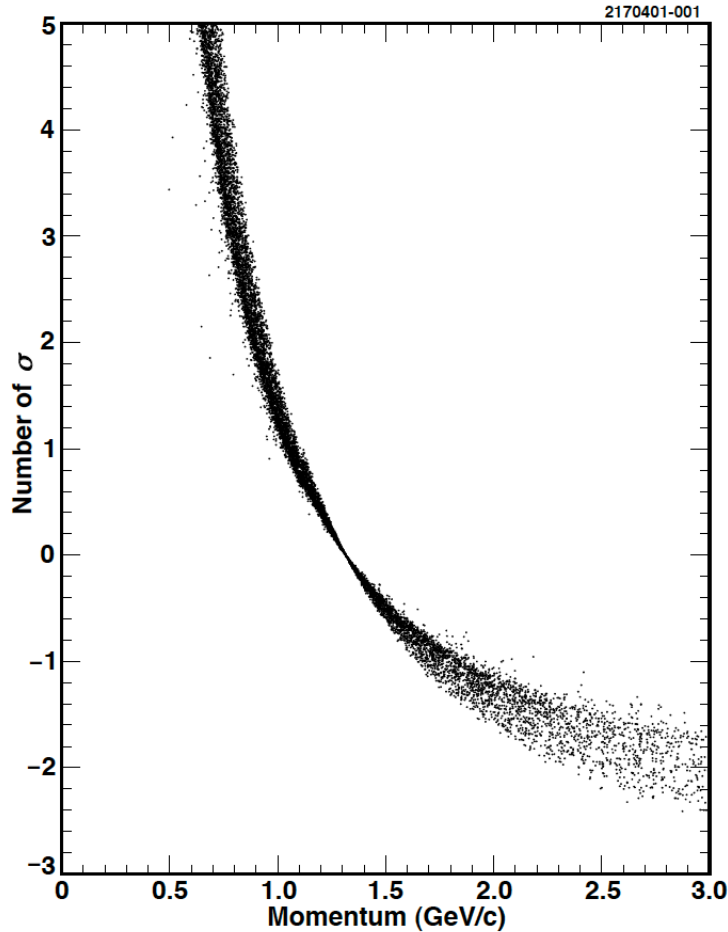
Figure 2.5: Statistical separation of pion and kaon tracks by dE/dx, obtained with tagged D^0 decays.

2.2.2   RICH Detector

The Ring Imaging Cherenkov Detector, which is called RICH detector, covered about 83% of the entire solid angle. It is constructed between the new drift chamber

and the old crystal calorimeter.

Emission of light by charged particle moving faster than the speed of light in a dense medium was discovered by Pavel Cherenkov and explained theoretically by Frank and Tamm [21]. Light will be emitted in a cone around the direction of the charged particle's path when they are traveling in the medium. The RICH detector determines the identity of charged hadrons by measuring the angle of emission of Cherenkov light. The emission angle of the light in matter is given by the following formula

$$cos\theta = \frac{1}{n\beta}, \tag{2.4}$$

In the equation, β is the ratio of velocity to c, and n is the index of refraction for the medium (radiator). If the momentum of the particle is measured independently and the angle of Cherenkov light emission is also reconstructed, the following equations are used:

$$\beta = \frac{p}{E}, E^2 = m^2 + p^2, cos\theta = \frac{1}{n}\sqrt{1 + \frac{m^2}{p^2}}, \tag{2.5}$$

The E, p, m in the equation refers to the energy, mass and momentum of the charged particle. A likelihood can be constructed by this information for particle identification.

A Ring Imaging Cherenkov Detector consists of a radiator, which is used to generate Cherenkov photons, an expansion volume (to allow photons to separate) and the radiator is made of LiF. The RICH detector schematic is shown in Fig. 2.6. LiF is expensive, but it is chosen as the radiator because it has the lowest dispersion in the wavelength band of the detector quantum efficiency [22].

The radiator is about 1 cm thick, followed by a 15.7 cm expansion volume. There are 14 rows of crystals, with a small change in construction between those in the center and those near the edges. In the center, the rows have sawtooth surfaces,
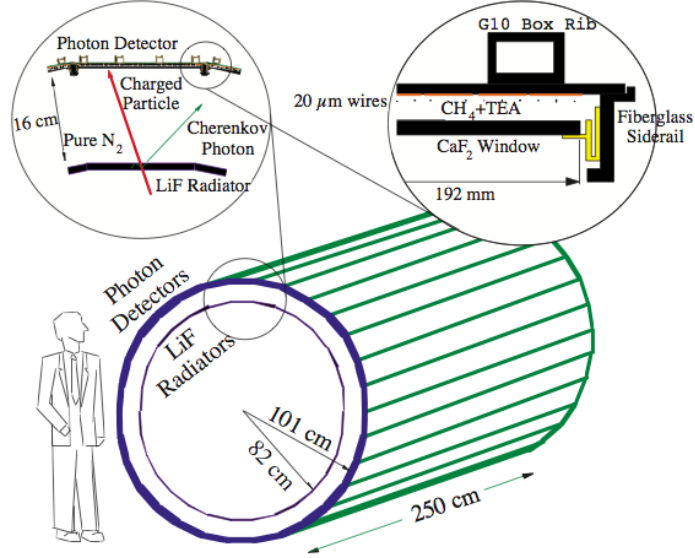
Figure 2.6: Outline of the CLEO-c RICH detector design.

which prevent internal reflection. At the edge, the rows are smooth. The photons would travel through the expansion gap filled with nitrogen and enter the multi-wire proportional chambers through CaF_2 windows.

The multi-wire chamber is the photon detector. It is filled with a mixture of TEA (triethylamine), which is a gas with a high ionization cross section for UV radiation, and methane gas. When UV photons travel into the gas mixture, the photoelectrons are created and then multiplied by high voltage wires, and finally collected at the cathode and converted to electronic signals.

The RICH uses the χ^2, which is calculated from the likelihood ratio, to identify charged particles. Given particle species i and j, the calculation of the χ^2 is based on the following equation:

$$\chi_i^2 - \chi_j^2 = -2\ln(L_i) + 2\ln(L_j), \tag{2.6}$$

with L_i being the combined probability that the recorded photons associated with

the track were originated by a particle of a given mass

$$L_i = \Pi_k P(\theta_k | m_i).$$

Then the separation for kaon and pion would be $\chi_K^2 - \chi_\pi^2$. Fig. 2.7 presents the measured fraction of kaons (pions) as a function of the cut on $\chi_K^2 - \chi_\pi^2$. As shown in the figure, for example, with a cut $\chi_K^2 - \chi_\pi^2 < 0$, one can detect 92% of kaons produced within the active solid angle, with a pion fake rate of about 8%. This was measured with momenta from the kaon radiation threshold to about 2.7 GeV. The theoretical separation of charged particles due to the RICH alone is shown in Fig. 2.8.
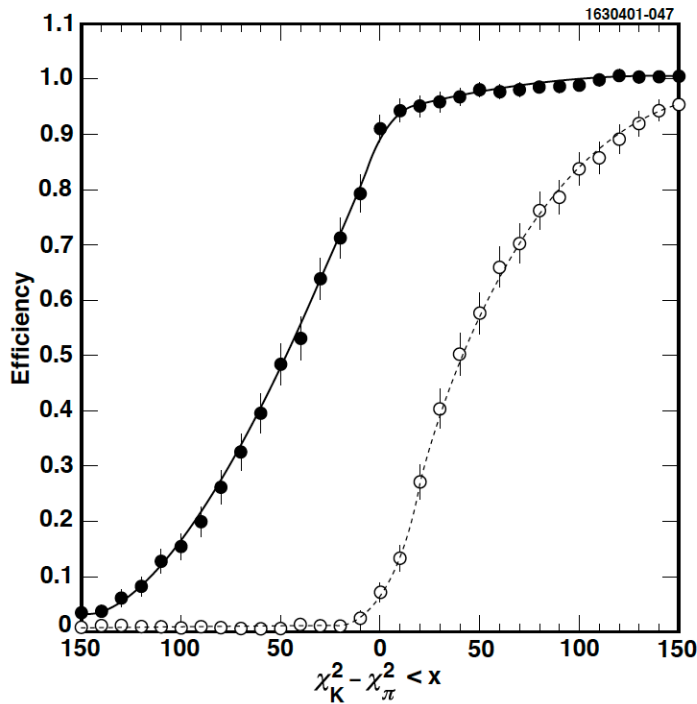
Figure 2.7: Kaon efficiency and pion fake rate measured for various cuts on $\chi_K^2 - \chi_\pi^2$ for track momentum from 0.7 GeV to 2.7 GeV for CLEO-c RICH detector. The solid black points show the kaon efficiency. The white points are the pion fake rate. The plots were obtained with a D^0 tagged decay sample.

In summary, RICH is a good supplement for high momenta tracks, but the dE/dx will do a better job at low momentum.
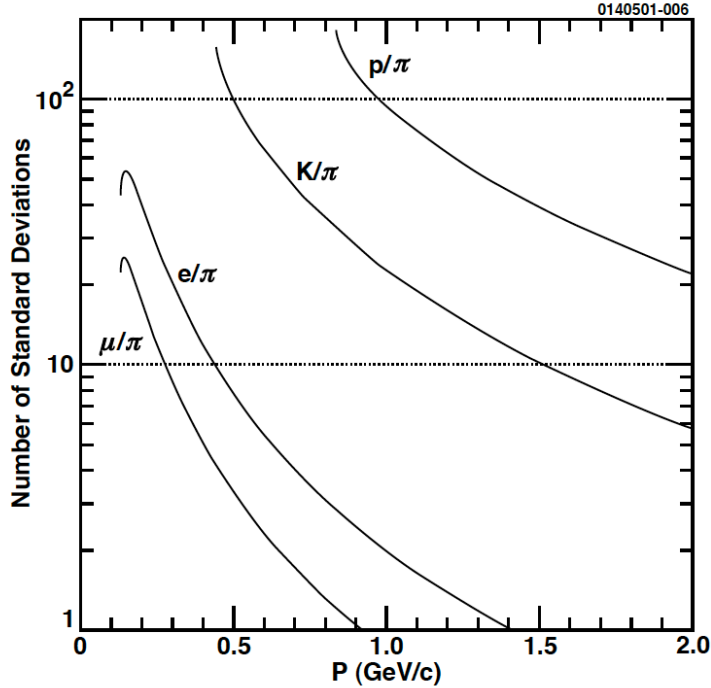
Figure 2.8: Theoretical separation of charged particles by the CLEO-c RICH detector versus track momentum. The intersection of the dotted lines with the theoretical curves represent the minimum radiating momentum for both particles emitting Cherenkov photons in the LiF radiator.

2.2.3 Crystal Calorimeter

The Cesium iodide electromagnetic calorimeter (CsI calorimeter) plays an important role in event classification, π^0 reconstruction and hardware trigger in CLEO. The CsI calorimeter measures energy deposit. A fixed fraction of the deposited energy is converted into visible light, and visible photons are counted to provide the experimental energy measurements. For electrons and photons, essentially all their energy is released in the calorimeter, so that the measured energy is close to the true particle energy.

The calorimeter consists of 7800 thallium-doped Cesium Iodide (CsI) crystals like the one shown in the Fig. 2.9. Each CsI block is approximately $5 \times 5 \times 30$ cm long.

Fig. 2.10 shows a cross-section of the CLEO-c detector. The CLEO Crystal Calorimeter consists of a barrel section and two endcaps, together covering 93% of
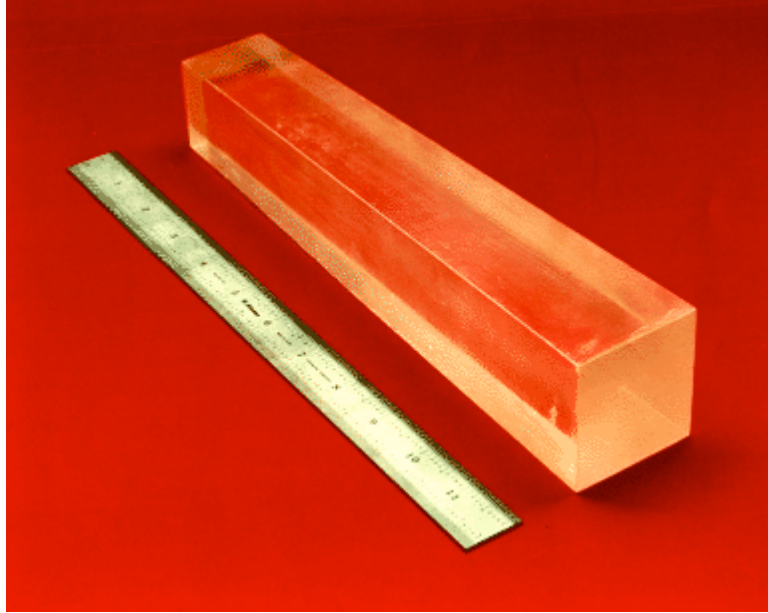
Figure 2.9: CLEO-c CsI crystals unit.

the solid angle. The barrel portion of the calorimeter, which is almost unchanged since CLEO II, contains 6144 crystals arranged so that all crystals point at or near the IP, covering totally about 80% ($|\cos\theta| < 0.8$) of the solid angle. The endcaps (region with $0.8 < |\cos\theta| < 0.93$) were constructed for CLEO III to accommodate the new CESR interaction region quads.

The efficiency and energy resolution in the endcaps are worse due to intervening materials. It should be mentioned that the transition region between barrel and end cap crystals also has worse resolution, and generally, photon candidates in that region are not used for analysis.

Charged particles like electrons will deposit energy through electromagnetic radiation, which is also called "Bremsstrahlung". This type of radiation depends on the relativistic factor γ^2, so that only electrons predominantly lose energy this way. The high energy photons emitted by the electron convert into electron positron pairs, which will generate more bremsstrahlung, effectively generating a cascade (or "shower") of typically hundreds of particles at CLEO-c energies. All fast electrons and positrons will excite nearby crystal atoms. After a few nanoseconds, the atoms in crystals will de-
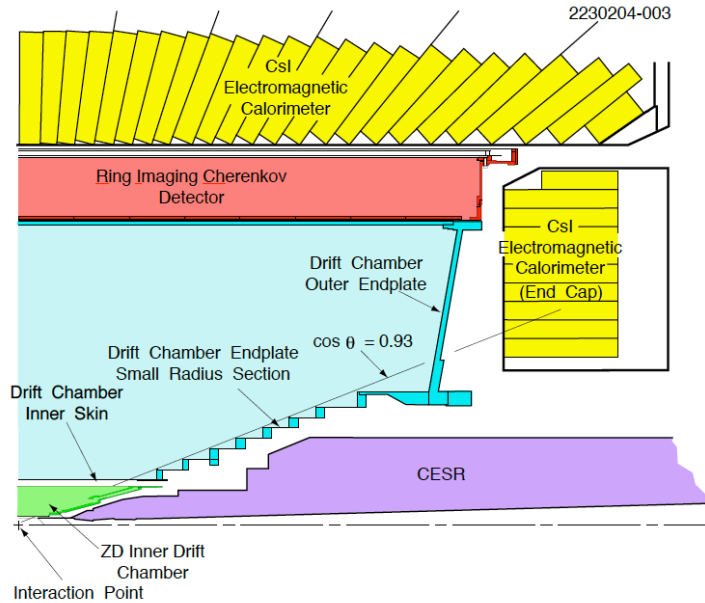
Figure 2.10: Cross-section of detector system image showing CLEO-c detectors.

excite emitting visible photons. Photon-initiated showers are similar in shape and size to electron showers. The first step is through pair creation predominantly, and then the daughter electron and positron will themselves generate other bremsstrahlung photons, and a shower is generated.

Charged particles like hadrons will lose energy much more slowly than electrons because they have a much smaller γ. Strong interaction with nuclei in crystals will generate various types of showers. Predominantly, nuclear fragments will be produced in various directions, creating a much broader shower than in the electron or photon cases. Rarely, neutral pions could be produced, which then decay to photons and generate two showers. These photon pairs then deposit all their energy and effectively mimic electrons.

Generally, a hadron shower will spread over several neighboring crystals. The sum of the energy detected by each crystal in a contiguous cluster is used to evaluate the deposited energy. This sum of energy from multiple crystals is called the energy clus-

ter, with the restriction that every one crystal should have no more than 2 segments away from other crystals within a cluster.

In CLEO, there is a special algorithm to separate hadronic and photon showers. The starting point is the highest energy crystal in the cluster. The energy deposition is then calculated from the sum of the 9 (25) crystals including the central one (see Fig. 2.11). If the ratio $E_9/E_{25} > 0.95$, the shower is classified as a photon shower. If one of the neighboring crystals is used in more than one clusters, then the energy is also split among different clusters.
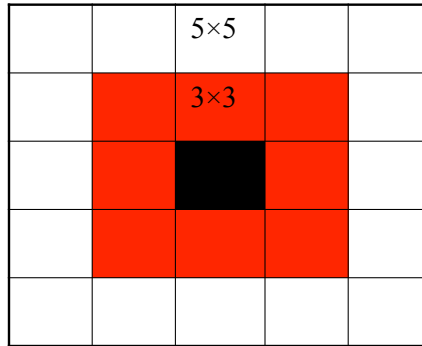
Figure 2.11: Depiction of the main hadron/photon shower separation algorithm. The inner energy deposition is in 9 crystals, the total deposition in 25 crystals.

This method optimizes hadron/photon separation, while efficiently separating nearby showers. The angular resolution is around 10 mrad. The energy resolution is about $1.3\%/\sqrt{E}$, with E expressed in GeV.

The CsI Calorimeter in CLEO-c is important because it is the only detector that measures neutral particles (photons). The abundant π^0 hadrons decay into two photons 99.7% of the time, and the CsI is the sole method of identification. The overall mass resolution for π^0 reconstruction ($\pi^0 \to \gamma\gamma$) from CsI Calorimeter for moderate

momentum (p > 0.3 GeV) is shown in Fig. 2.12.
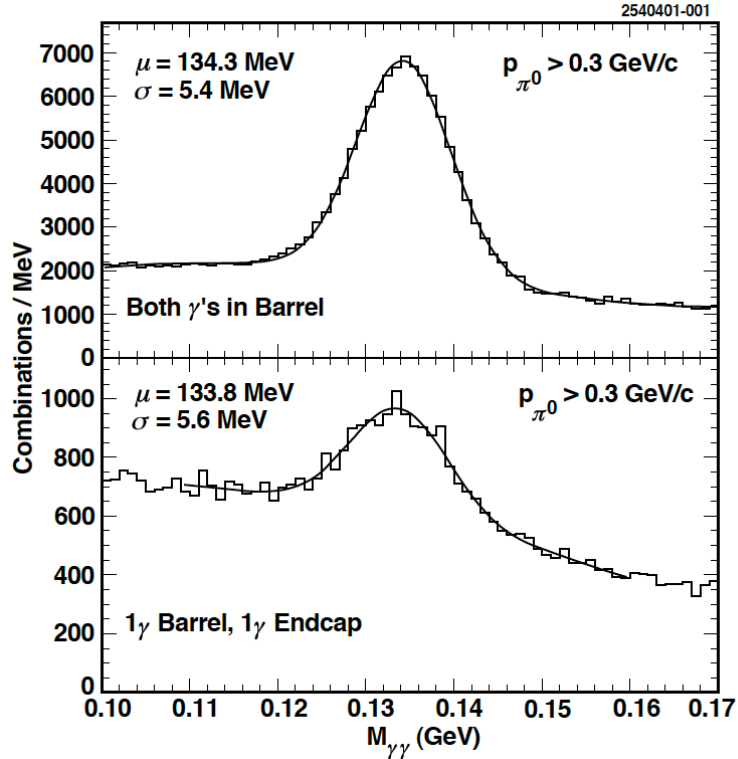
Figure 2.12: π^0 reconstruction resolution by CsI calorimeter from CLEO III data.

2.2.4   Cylindrical wire vertex chamber

The low mass cylindrical wire vertex chamber, which is called ZD, replaced the SVD in CLEO-c. It occupies radii from 4.1 cm to 11.8 cm to the center of the Beam Pipe. The materials of cylindrical wire vertex chamber are gold-plated aluminum field wires and gold-plated tungsten sense wires, same as the materials used in the main drift chamber. The cylindrical wire vertex chamber has 6 layers, and similar to the SVD, they were expected to provide position of charged tracks within $|\cos\theta| < 0.93$ (θ is the angle between charged tracks to beam pipe). The momentum resolution of the cylindrical wire vertex chamber is better than the SVD, however, the space resolution is not as good as the SVD, since it is only about 680 μm in the z direction.

2.2.5 Superconducting Coil

The CLEO III superconducting coil provides a uniform 1.0 T magnetic field parallel to the beam over the full volume of the inner tracking, central tracker, RICH and CsI system. The coil has an inner diameter of 2.9 meters and 3.5 meters length.

In CLEO-III, the magnetic field was 1.5 Tesla. The reduction of magnetic field is useful to improve the reconstruction efficiency at low momenta. Particles helices will be longer, and intersect the trackers, whereas at high magnetic field they could curl very close to the beam pipe and be lost.

2.2.6 Muon tracking

Since muons are highly penetrating charged particles, they have minimum ionization in the calorimeter. CLEO-c has special muon chambers located outside the CLEO-c detector system. The main components of the muon detector are the iron return yoke of the superconducting coil and interleaved wire chambers. The iron in the return yoke stops all other particles from going into muon chambers.

But the muon chamber is not used in CLEO-c analysis because the muon detector performs poorly for muons with momenta below 1GeV. This device is not used in the analysis described below.

2.3 CLEO-c data acquisition

The process by which data are collected in CLEO-c include a Trigger System (TRIG), Data Acquisition System (DAQ), and is designed to maximize the data collection efficiency and purity. We will discuss these two special procedures in this section.

2.3.1   Trigger system

The CLEO-c trigger system performs fast pattern recognition to find tracks in the drift chamber (tracking trigger) and shower clusters (calorimeter trigger) in the calorimeter.

The tracking trigger consists of two parts: axial and stereo. The tracking trigger will check the chamber output for tracks signals and consider axial and stereo separately. The axial trigger will check all 1696 axial wires within sixteen radial layers for those hit patterns that are consistent with tracks of momentum greater than 200 MeV. The stereo tracking has 8100 wires from drift chamber. Since there are too many wires, the stereo tracker reads out wire hits by 4×4 blocks of wires and a hit must be present on at least three out of four layers to satisfy a block pattern.

The calorimeter trigger incorporates digital and analog electronics to provide those pipelined triggers information every 42 nanosecond. The latency is about 2.5 μs. Digital field programmable gate arrays are used extensively to categorize and filter the calorimeter energy topology and the analog processing was employed to address quantization errors caused by split energy depositions in adjacent calorimeter crystal cells.

Data from the drift chamber (tracking trigger) and calorimeter (calorimeter trigger) are processed in separate VME crates by appropriate circuits to get basic trigger primitives (like track count). These information from both systems are correlated by the so-called "global trigger", which generates a pass strobe every time a valid trigger condition is satisfied. In such case, a "Level 1 Pass" signal will be sent to the DAQ and all information of this event will be saved; otherwise, this event will be rejected and will not have further processing by DAQ. There are four crystal calorimeter (CC) analog trigger crates, which have no fast digital logic and thus are not read out by the DAQ system.

There exists also a Level 2 trigger which has the same functionality as described

Name	Definition	Prescale	Relative Rate
Hadronic	$N_{axial} > 1$ and $N_{CB\ low} > 0$	1	0.41
μ-pair	two back-to-back stereo tracks	1	1.0
Barrel Bhabha	back to back high showers in CB	1	1.0
Endcap Bhabha	back to back high showers in CE	8	0.23
Electron + track	$N_{axial} > 0$ and $N_{CB\ med} > 0$	1	1.48
τ/Radiative	$N_{stereo} > 1$ and $N_{CB\ low} > 0$	1	2
Two Tracks	$N_{axial} > 1$	10	0.69
Random	random 1 kHz source	1000	1

Table 2.1: Current definitions of CLEO triggers. "CB" in the table refers to Crystal Barrel and "CE" stands for Crystal Endcap

for LEVEL 1 but with much higher resolution. For example, track segments at this level encompass all layers, not just blocks.

The signals from all detector subsystems reside in data boards in readout crates: 8 RICH VME crates, 8 DR3 Fastbus crates, 4 CC Fastbus crates, 1MU Fastbus crate, and 5 VME trigger crates. The Data-Mover reads out all the data boards into ring buffers, do any necessary sparsification (SPA) and put the event buffer into an output ring buffer to be shipped via fast ethernet, through the fast ethernet switch, to the event builder consumers. All signals will then be transferred to Level 3, the final trigger. Upon acceptance by Level 3, all the event fragments are then transmitted from the crates to the Event Builder.

In CLEO-c, trigger rate is about 40 to 45 Hz at $L = 5 \times 10^{32} cm^{-2} s^{-1}$ and there are about 8 triggers working as event selectors (totally 24 available) with some special criteria, shown in Table. 2.1.

2.3.2 Data Acquisition System

The CLEO data acquisition system writes events that pass all trigger levels. The run control, alarm and message handling systems handle all tasks related to shift duties.

Fig. 2.13 shows the overview of the CLEO III Data Acquisition System (DAQ).The

CLEO-c system is identical except for replacing the SVD with the Cylindrical wire chamber (ZD).

The figure shows the data flow from data board buffer of each detector (total about 400,000 detector channels have to be digitized) to computers for final recording. The trigger lines could activate the DAQ during the data flow, and then those signals will be transferred to the Event Builder, where all received signals from all detector channels would be constructed as one event. Completely assembled events are then transferred to storage and part of the data will be analyzed online by monitor programs to discover possible problems and ensure the quality of the data written on the tape.

The performance of the DAQ is evaluated based on the data transferring time, which should be small to minimize CLEO-c dead time. Dead time is defined as the time between the end of digitization processing and receiving triggers signal. All events will be lost during this time.

There are two main factors that affect the transferring rate in CLEO-c, one is data read-out, while the other one is data transferring bandwidth. The data transferring bandwidth depends on the event size. The data read-out rate is generally calculated by using the total cross section, trigger efficiency and luminosity. This analysis uses $\psi(3770)$ data, with a total cross section of about 580nb. 90% of this cross section is Bhabha scattering, while the other 10%, which is about 50 nb, is from charm particles and continuum events. Assuming 100% trigger efficiency, the read-out rate is about 80 Hz for an event size of 25 kB and dead time of about 0.2%.

2.4   CLEO data sets and analysis software.

CLEO-c has collected data at several beam energies. There are about 818 pb^{-1} data on the $\psi(3770)$, and over 30 million $\psi(2S)$ decays. We also have a data set at the $\psi(3095)$, data at continuum below the $\psi(2S)$, E_{cm} at 4260 MeV and 586 pb^{-1}

data with E_{cm} at 4170 MeV for those D_s physics.

CLEO developed a set of C++ libraries for analysis in CLEO. The bulk of the data is reconstructed with a special software in CLEO library, named "pass2". This program finds and measures all the tracks and showers. The analysis presented in Sections 3 and 4, and also most other charm analysis in CLEO, use a reduced data set called "D Skim". The D Skim processes those pass2 events so as to reduce the data set by rejecting uninteresting events with minimal quality cuts. The whole event is saved when an interesting candidate is found.

2.4.1   Monte Carlo data

Monte Carlo simulation is one of the most important analysis tools in not only high energy physics, but almost all science research area. One can calculate selection efficiency, study the background, and optimize cuts by analyzing Monte Carlo data. In CLEO, the simulation of Monte Carlo data include two parts: EvtGen and Detailed Simulation. In the first step, EvtGen simulates how the initial state $\gamma^{\star}$ decays to final particles. In the second step, the effects of the CLEO-c detector on the particles produced in the first step are simulated.

There are two kinds of Monte Carlo data in CLEO, generic MC and signal MC. Generic MC data, which is produced by the CLEO collaboration, includes all known physics. Those charm decay events simulate decays from $D^0 \bar{D}^0$ and $D^+ D^-$ pairs based on world averages of branching ratios and other decay parameters from Ref. [11]. The Generic MC is also D Skimmed so that one could analyze generic MC data in same way. Signal Monte Carlo data is simulated by the particular researcher based on his or her analysis interest. One can generate decays that have not been previously observed, or decays that are in the Generic MC data, but not with sufficient statistics, or perhaps with a different decay distribution.

2.4.2   Event Display

CLEO also has a special analysis tool called "Event Display", which is a set of processors that draw CLEO data on the screen event by event. It is very useful for CLEO analysis especially for data quality check and background identification.

Fig. 2.14 shows one typical event display for CLEO-c data event in the $x-y$ plane. Each curved line in the figure stands for a charged track, and small circles near the edge are showers, with energy deposition proportional to the area of the circle. The event can be displayed also in the $x-z$ and $y-z$ projections.

2.4.3   Analysis software

In this Section, commands or source code are shown directly, and they are in *italic*.

CLEO-c library runs on GNU/Linux system and the source code is written in C++. Typically in each analysis software package, ("Processor" for example), there are two important files that need to be modified: *Processor.cc* and *Processor.h*. The selection and calculations are done in *Processor.cc*, and *Processor.h* are where most of the parameters and *Ntuples* (see below) are defined.

CLEO-c has a structured source of analysis code available. The analysis software package with different structure could be created automatically by a simple command *mkproc* with different selecting parameters. For example, a command *mkproc -dtag Processor* could create a software package with the name Processor (with *Processor.cc* and *Processor.h* files in this package) and with structure *Dtag* ready to compile. CLEO-c also has a special server with name *lnx134* for compiling purpose. The command *c3make*, which calls the GNU compiler and a special file called *Makefile* , directs the compilation. And *Makefile* is also included in the software package automatically.

A compiled software package can be run by control file, generally with extension

tcl within framework *suez.* In the control file, the software package points to particular data or MC data, and also some other package can be loaded, (for example electron ID, which is *eid* loaded in Tcl script). CLEO also provides servers for those long processing software (generally more than an hour). Those processing jobs could be submitted via the Grid Engine queueing system by using a simple command *qsub.* At the same time, some control command are used to determine on which particular server you want to run the job. The control command is something like *arch=lx24-x86.* Commands such as *qstat* help check running jobs and *qdel* will delete un-useful jobs.

2.4.4 Output

CLEO analysis output is saved in two different files, *log* and *root* files. *log* files saved information during processing of software package and is always checked for processing status of source code or for debugging. The *root* files contain histograms and data information for final analysis. The data structure of data in *root* is the Ntuple, which can store all the relevant quantities in an event. Storing Ntuples allows us to make histograms of a variable and easily change the histogram endpoints and binning. One could also make two dimensional histograms and histograms of a certain subset of events by some simple cuts on variables.

There are two ways to make *root* files, one can simply tell *suez* to make a *root* file rather than a PAW/MN_FIT files, and the other is to use ROOT within *suez* to create files. After one obtains the output files, some tools are needed to make further analysis and make plots. In this analysis, ROOT is used for making plots and fittings.
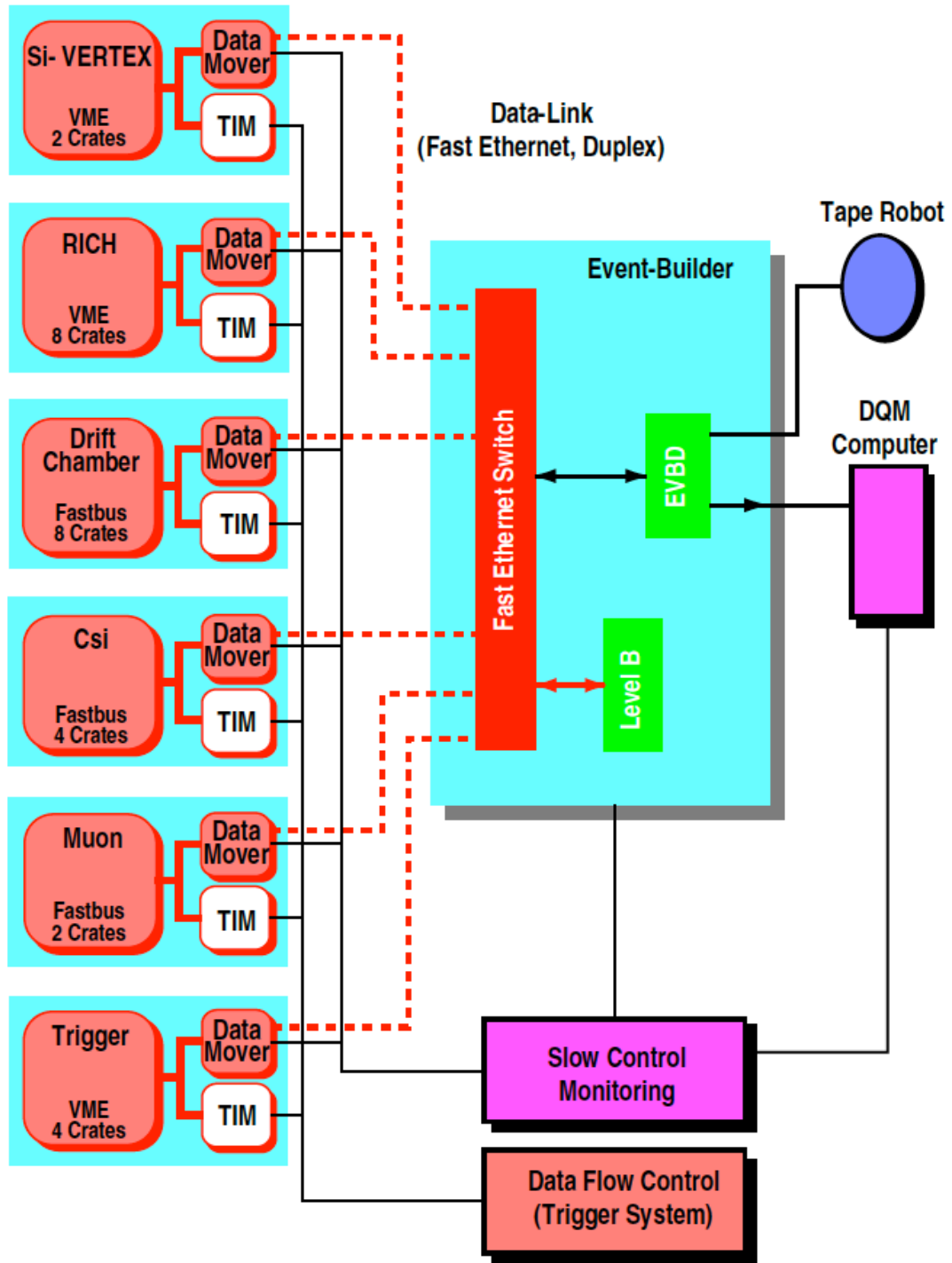
Figure 2.13: Overview of CLEO III Data Acquisition system
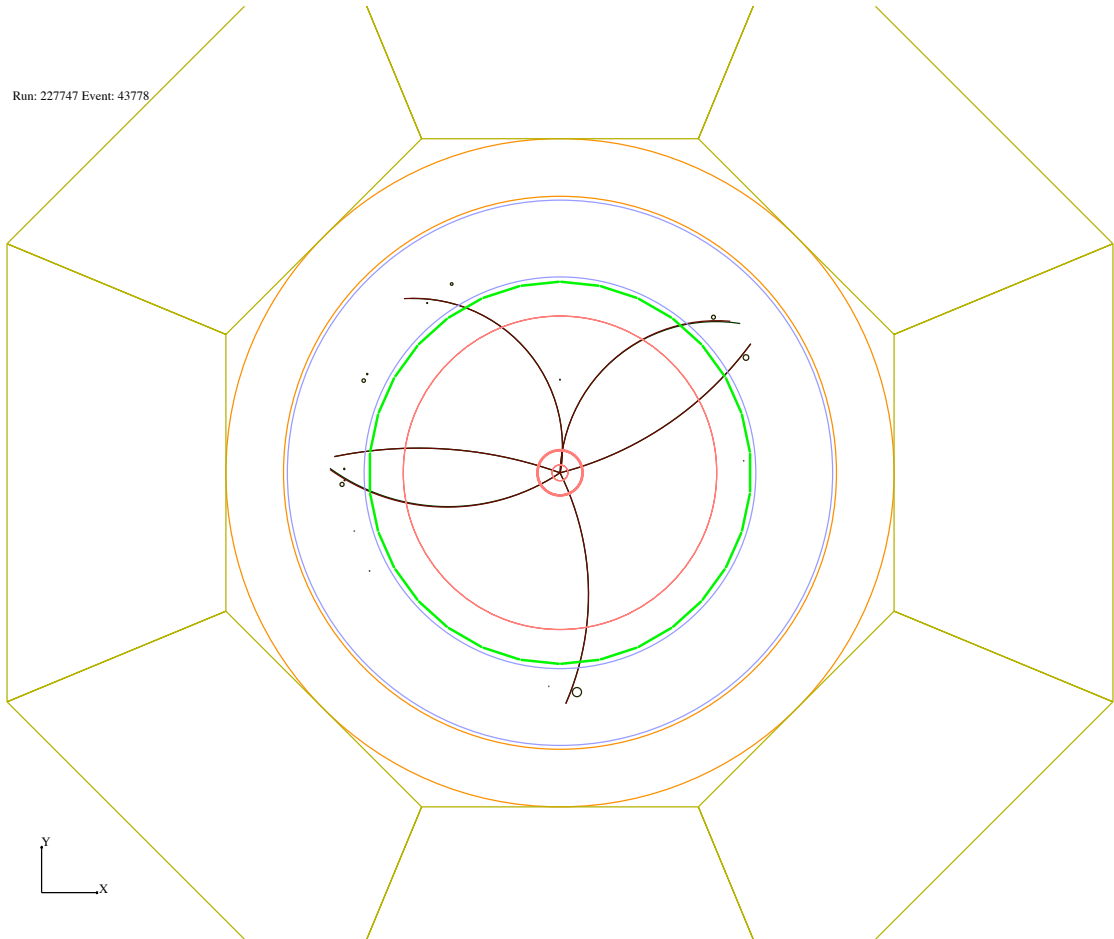
Figure 2.14: Event display for one CLEO-c event in the $x - y$ plane

Chapter 3:   Experimental Method

3.1   Overview

This Chapter briefly describes the method of selection of the final states if interest. All data in this analysis were taken at $\sqrt{s} = 3770$ MeV. This is at the the resonance $\psi(3770)$ which predominantly decays to $D\bar{D}$ pair (either $D^0\bar{D}^0$ or D^+D^-). Both D^+ and D^- are analyzed but charge invariance is assumed, so that all branching ratios are quoted as branching ratios of the D^+.

It is important to notice that the reactions involving charmed mesons at this energy are exclusively

$$e^+e^- \to D^+D^-. \tag{3.1}$$

No other particle is present in the final state. Conservation of 4-momentum implies that both mesons have energy equal to the beam energy, and opposite momentum.

Both single tag and double tag techniques are used in selecting our signal. In single tag technique, a combination of particles consistent with the final state to be studied is selected, with total energy within 20 MeV of the beam energy, or $|\Delta E| < 20$ MeV. The combination is further kinematically fit to the nominal beam energy value, to obtain M_{BC}, the best possible measurement of the invariant mass, if the process is the one described by Eq.3.1.

Once a signal statistics N_{sig} is obtained, the branching ratio for the single tag method, B_s, is obtained through the following equation

$$B_s = \frac{N_{sig}}{\epsilon N_{DD}}. \tag{3.2}$$

The number of produced D^+D^- pairs, N_{DD}, is obtained from Ref. [23]. Our sam-

ple contains about 2.354×10^6 D^+D^- pairs. ϵ refers to the reconstruction efficiency, which is computed by Monte Carlo simulation of the detector, as the ratio of generated and reconstructed events. Details of the efficiency are discussed in Chapter 4. This method provides the best statistics but also significant backgrounds. Therefore, a double tag technique is also applied to extract the same branching fraction and cross check the result.

In double tag mode, which has lower backgrounds but lower statistics, both D^+ and D^- are reconstructed, one with the final state of interest, and the other with one of six high statistics, low background modes (discussed below), called the tags. To extract a branching ratio using the double tag method, the following equation is used

$$B_d = \frac{N_{sig}}{\epsilon N_{tag}}, \tag{3.3}$$

where N_{sig} and N_{tag} are the yields from the signal side and tag side of the event. This method loses about a factor of five in statistics but the backgrounds are lower, because all tracks and showers in the tag combination are eliminated from consideration when searching for the signal. The backgrounds that are suppressed are of the combinatorial type.

When the decay being investigated is of the type $D^+ \to \phi X$, the branching ratio is corrected by the known branching ratio $\phi \to K^+K^-$, which is 0.489 [11]

$$B_{d,s}(D^+ \to \phi X) = \frac{B_{d,s}}{B(\phi \to K^+K^-)}. \tag{3.4}$$

3.2   Data Samples

818 pb^{-1} of data produced in e^+e^- collisions at CESR near the center-of-mass $\sqrt{s} = 3770$ MeV, were analyzed. Data sets used in this analysis are dataset 31-33, 35-37 and 43-46 in CLEO-c.

Two kinds of Monte Carlo data were used. The Generic Monte Carlo (GENMC), was generated by the CLEO-c collaboration at large and contains all known charm particle events. The GENMC data used in this analysis is generic MC date set 43-46, which are 20 times the number of events corresponding to the real data set 43-46, and about 18 times the total data set. The other is signal Monte Carlo, which is generated for specific final states. One D is generated according to the specified final state, while the other side will decay based on the same algorithm that generates both D in the GENMC. In the analysis several kinds of signal MC data were generated. They are listed in Table 3.1.

Table 3.1: Modes of signal Monte Carlo generated in the analysis. All modes were generated according to a phase space distribution.

signal MC hadronic modes	number of events
$D^+ \to K^+K^-\pi^+\pi^0$	10^5
$D^+ \to \phi\pi^+\pi^0$	10^5
$D^+ \to K^+K^-\rho^+$	10^5
$D^+ \to \phi\rho^+$	10^5
$D^+ \to K^+K^-K^+$	10^5
$D^+ \to K^+K^-\pi^+\pi^+\pi^-$	10^5

3.3   Final State Reconstruction

In both single tag and double tag, each charged track as well as π^0 need to be identified and its 4-momentum has to be measured. In this section, a brief description is given of how the tracks and π^0 are selected and identified in the analysis.

3.3.1   Charged track selection and efficiency

Tracks are efficiently reconstructed in CLEO-c, but some cleaning cuts are needed to minimize unwanted backgrounds from cosmic rays, or to eliminate random coincidences and multiple reconstructed tracks from a single low momentum particle going

through multiple helical revolutions in the CLEO-c magnetic field("looper"). The cuts are listed:

1. TRKMAN approved. TRKMAN is a general cleaning routine that insures that the track has a minimum number of hits and is not a looper.

2. $0 < \chi^2 < 100000$. A good quality track should have positive but low χ^2.

3. Ratio of hit ≥ 0.5. This cut means no less than half of cells crossed by tracks should have a hit associated with that track.

4. also require the distance of closest approach to the interaction point in the transverse plane $|d_0| <$0.005 m. This and the next cut minimize the effect of tracks that have undergone large angle scattering in the detector material. This and the next two cuts also minimize cosmic backgrounds.

5. Distance closest approach to IP in the longitudinal direction $|z_0| <$0.05 m.

6. Track has to have momentum greater than 50 MeV but less than 2.0 GeV. Low momentum tracks are poorly reconstructed, while tracks from annihilation events can not exceed the beam momentum.

7. $|\cos\theta| <$0.93, where θ is the angle that the particle makes with the beam. Tracks near the beam pipe are poorly reconstructed.

Track masses are assigned as follows. In CLEO-c, as discussed in Chapter 2, two particle identification devices are used to separate pions from kaons:

1. the Drift Chamber measures dE/dx (energy loss per unit length)

2. the RICH measures Cherenkov light to identify charged particles

For the purpose of differentiating pions and kaons, the dE/dx (with information p$ionsigma$ and k$aonsigma$), and RICH (with p$ionLogLikelihood$ and k$aonLogLikelihood$) will create the combined figure of merit

$$L = pionLogLikelihood - kaonLogLikelihood + pionsigma^2 - kaonsigma^2. \quad (3.5)$$

L is required to be less than zero for the track to be a good pion. Kaon candidates are selected as good tracks with dE/dx within 3σ of the kaon hypothesis. The combined identification has pion or kaon efficiency greater than 85% and also a probability of kaon contamination of less than 5% [24].

3.3.2 Shower selection

The Electromagnetic calorimeter measures the photons energy. Showers are reconstructed by converting the amount of detected light into an energy measurement. Electromagnetic showers have typical transverse spreads smaller than the size of a crystal, with low but long tails. The algorithm chooses an isolated cluster of crystals with pulse heights exceeding 10 MeV in equivalent energy. Each shower is then characterized by using E9OE25 (discussed in Chapter 2) that a good shower should has E9OE25 no less than 0.95.

Some showers are associated with charged tracks. These showers are initiated by hadrons and their lateral spread is much greater than that of true photons, so they are rejected by the 9/25 cut described above, but a minimum distance (20cm) to a projected track entry point is also required. There are also some pulse heights which are not due to any particle but simply to noisy photodiodes in the back of a crystal. Finally, low energy showers are more likely to be background, as are showers at angles where there is a lot of material in front of the calorimeter. The following cuts specify photon selection:

1. shower is not hot and no TrackMatch.

2. E9OE25 OK.

3. Good shower has to have energy greater than 50 MeV, good Barrel or Endcap.

3.3.3 π^0 selection and efficiency

π^0 are reconstructed by using two good showers since π^0 are identified through their dominant decay $\pi^0 \to \gamma\gamma$.

The parameter used for good π^0 is "pi0.pullMass()" which is defined as

$$pi0.pullMass() = \frac{M - M_0}{\sigma}, \tag{3.6}$$

where M is the measured mass and M_0 the π^0 mass [11], and σ is the calculated mass resolution. The $|pi0.pullMass()| < 3$ cut is imposed.

The π^0 efficiency was studied previously with 281 pb^{-1} CLEO data[25]. The measurement was done by analyzing the decay $D^0 \to K^-\pi^+\pi^0$, where only the charged tracks are reconstructed in double tag mode. A missing 4-momentum consistent with the π^0 mass is required. This method finds indirectly the presence of a π^0, and where it hit the calorimeter. Fig.3.1 shows the π^0 efficiency difference between Monte Carlo and data with different mass cuts. From that analysis, it can be seen that the π^0 selection efficiency difference is around 94% with standard π^0 cuts. In this analysis, this is the largest systematic error if a π^0 is in the final state. The final quoted efficiency is corrected for this.

3.3.4 CLEO-c D tags

CLEO-c specific software[26] is the standard method to reconstruct D^+ mesons. Separate summary files are produced called D Skims, with events selected with minimal cuts. Each decay mode is given an identification number, which is also called
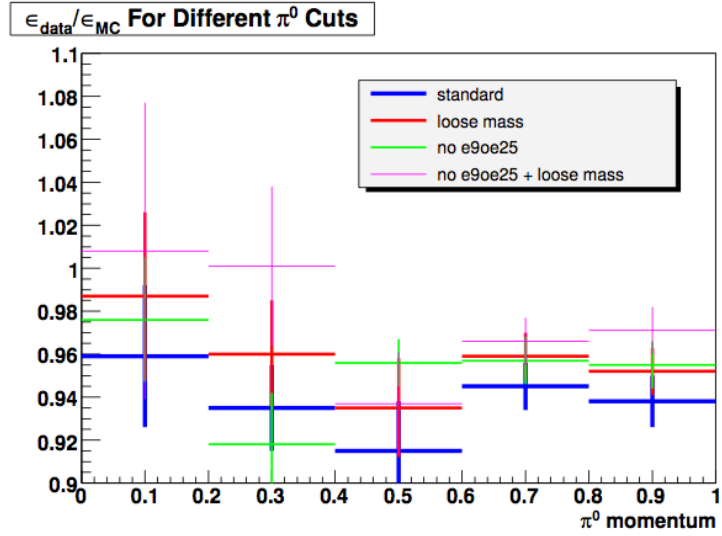
Figure 3.1: From Ref.[25]. π^0 efficiency ratio $\epsilon_{data}/\epsilon_{MC}$ for four different sets of π^0 mass cuts

enumeration code. A list of CLEO-c D^+ tag tables is shown in Table 3.2.

The six with the highest reconstructed statistics are selected to use in double tag mode in this analysis. These modes are listed in the Table 3.3

The $|\Delta E| < 20$ MeV cut is applied for tag selection too. If multiple tag candidates are present, the one with the minimum $|\Delta E|$ is selected.

Table 3.2: List of CLEO-c D^+ tag modes with measured width (in MeV), sorted by enumeration code

D^+	enumeration code	widths(MeV)
$K^-\pi^+\pi^+$	200	1.6/6/1
$K^-\pi^+\pi^+\pi^0$	201	1.8/9.6
$K_s^0\pi^+$	202	1.5/6.7
$K_s^0\pi^+\pi^0$	203	1.8/13
$K_s^0\pi^+\pi^+\pi^-$	204	1.5/4.9
$K^-K^+\pi^+$	205	1.5/4.8
$\pi^+\pi^0$	206	2/12
$K^+\pi^0$	207	2/12
K_sK^+	208	1.2/6.0
$\pi^+\pi^+\pi^-$	209	1.3/6.0
$\pi^+\pi^0\pi^0$	210	2.5/15
$K_sK_s\pi^+$	211	1.4/5
$K_sK^+\pi^0$	212	2.1/20
$K_sK_sK^+$	213	1.6/4
$\pi^+\pi^+\pi^-\pi^0$	214	1.5/11
$K_s\pi^+\pi^0\pi^0$	215	1.9/12
$K_sK^+\pi^+\pi^-$	216	1.6/5
$K_sK^-\pi^+\pi^+$	217	1.7/4.0
$K^-K^+\pi^+\pi^0$	218	2/10
$\pi^+\pi^+\pi^+\pi^-\pi^-$	219	1.4/4.7
$K^-\pi^+\pi^+\pi^+\pi^-$	220	1.4/3.9
$\pi^+\eta$	221	1.6/6
$K_s\pi^+\eta$	222	1.6/6

Table 3.3: D^+ tag modes used for double tag analysis.

6 hadronic modes	enumeration code
$D^+ \to K^-\pi^+\pi^+$	200
$D^+ \to K^-\pi^+\pi^+\pi^0$	201
$D^+ \to K_s^0\pi^+$	202
$D^+ \to K_s^0\pi^+\pi^0$	203
$D^+ \to K_s^0\pi^+\pi^+\pi^-$	204
$D^+ \to K^-K^+\pi^+$	205

Chapter 4: Measurement of Hadronic $D^+ \to KKX$ Branching Fractions

The final data analysis is presented here.

4.1 Mass fits.

All M_{bc} fits were done using the binned likelihood method, and all the fitting results are summarized in Table 4.9.

4.1.1 $D^+ \to K^+ K^- \pi^+ \pi^0$.

The fitting lineshape includes the effects of beam energy spread and experimental resolution. The background is described by an ARGUS function[27]

$$B(x; x_0, \epsilon, p) = Kx(1 - \frac{x^2}{x_0^2})^p e^{\epsilon(1 - x^2/x_0^2)}, \tag{4.1}$$

where K is a normalization parameter and m_0 is the endpoint given by the beam energy.

The signal is fitted by two functions, the first a core Gaussian $G(x; \sigma, M_D)$ with mean at the nominal D^+ mass M_D [11] and width σ. The second is the Crystal Ball function $C(x; \beta, n, m, s)$ [28], defined as follows. With the substitutions $r = (m - x)/s$ and $y = n/|\beta|$, and K being a normalization constant,

$$C(x; \beta, n, m, s) = K \begin{cases} e^{-r^2/2} & \text{if } \beta > r \\ y^n e^{-\beta^2/2}(y - |\beta| + r)^{-n} & \text{otherwise} \end{cases} \tag{4.2}$$
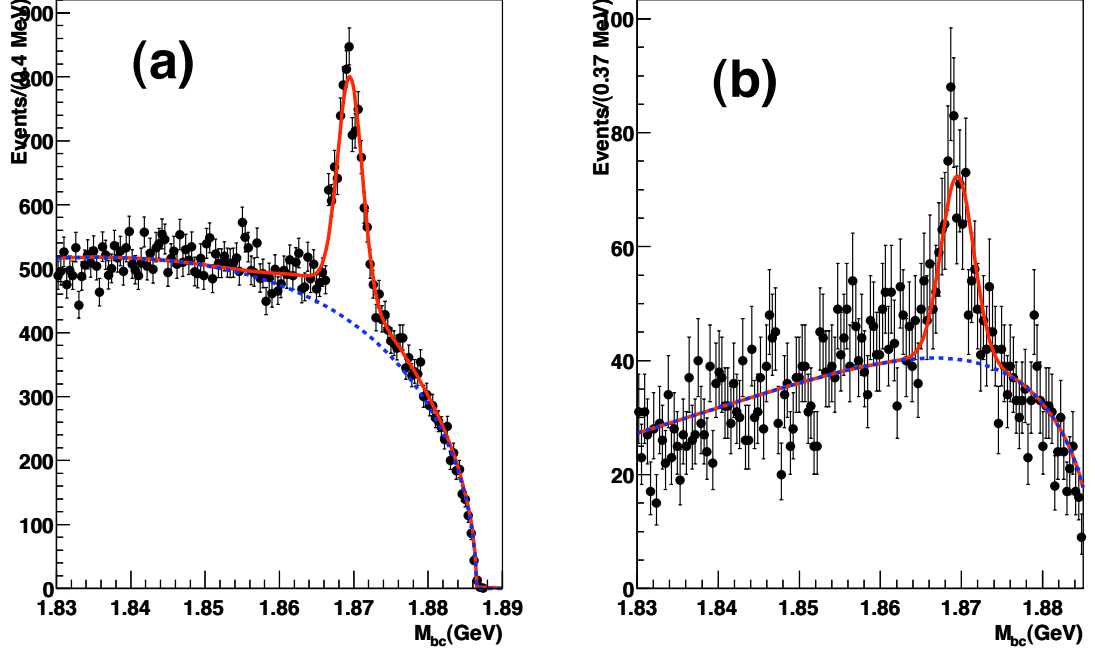
Figure 4.1: $D^+ \to K^+K^-\pi^+\pi^0$ mass spectrum and fit. a) single tag analysis; b) double tag analysis.

Therefore the overall fitting function is

$$F(M_{BC}; \alpha) = N_{tot}(f_1 G(M_{BC}; \sigma, M_D) + f_2 C(M_{BC}; \beta, n, m, s) + (1 - f_1 - f_2)B(M_{BC}; x_0, \epsilon, p)),$$
(4.3)

N_{tot} is the normalization of the spectrum, so that $N_{sig} = N_{tot}(f_1 + f_2)$ is the number of signal events.

The fitting result are shown in Fig. 4.1, for single and double tag respectively.

The fitting yields 5168 ± 100 events in the single tag D^+ peak and 507 ± 57 in the double tag peak, with χ^2/dof of 1.574 (149/95) and 1.014 (96.3/95) respectively.

4.1.2 $D^+ \to \phi\pi^+\pi^0$.

By side band subtraction of the background of M_{bc} (the sideband defined as the interval $1.84 < M_{BC} < 1.86$ GeV) one can obtain the spectrum of the two kaons mass, M_{KK} for signal D^+ events, which is shown in Fig. 4.2.

The spectrum is fit between 0.99 and 1.09 GeV to obtain the fraction of ϕ events. The chosen fitting function is a Gaussian convoluted with a relativistic Breit-Wigner squared amplitude $BW^2(x; M_0, \Gamma)$ plus a third order polynomial background

$$F(M; \alpha) = N_{tot}(f_1 K_1 \int G(x; \sigma, 0) BW^2(M - x; \Gamma) dx + (1 - f_1) K_2 \Sigma_i a_i M^i), \quad (4.4)$$

where K_1 and K_2 are normalization constants. The fitting yields 1383 ± 31 ϕ candidates.

The fitting function in Eq. 4.4 does not allow for interference terms between the resonant (ϕ) and non-resonant amplitudes. To check for possible interference effects, the data are refit with the fitting function

$$F(M; \alpha) = N_{tot} K \int Re\{(G(x; \sigma, 0)(\sqrt{f} BW(M - x; M_0, \Gamma) + \sqrt{(1 - f)}\Sigma_i a_i M^i) e^{i\theta})^2\} dx,$$

$$(4.5)$$

with $N_{sig} = N_{tot} f$. The result of the fit yields $\cos\theta = (+0.0100 \pm 0.0047)$, consistent with the incoherent sum of Eq. [?]. The interference term is an odd function near the peak, and its change on the peak normalization f, compared to the incoherent fit, is only +0.07%. This systematic error is far exceeded by other errors, and assuming the incoherent sum hypothesis simplifies our analysis.

4.1.3 Dalitz analysis

A 4-body final state like the one considered here has five degrees of freedom. A full analysis of the final state would imply the consideration of many amplitudes,
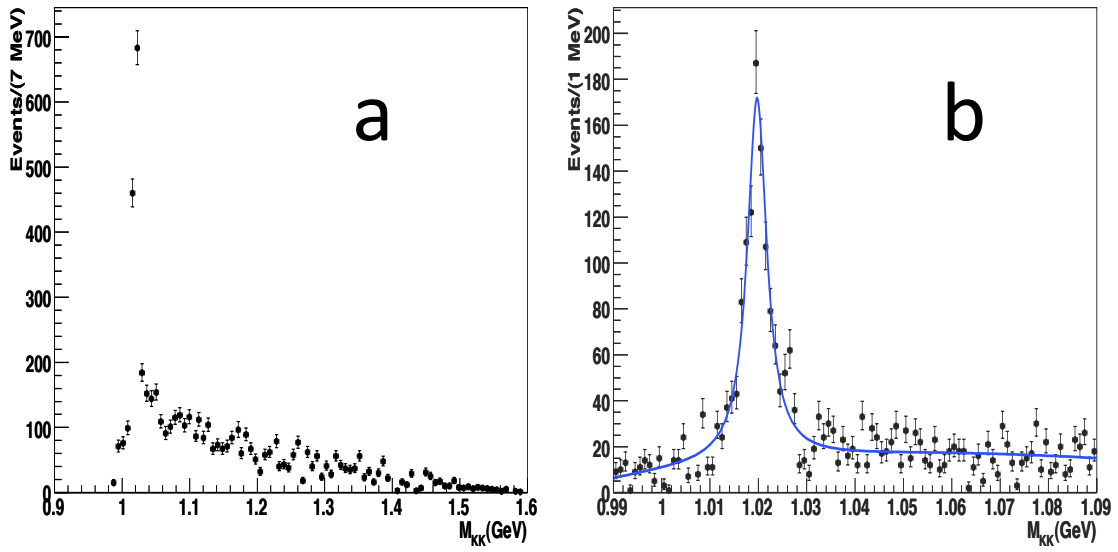
Figure 4.2: Single tag M_{KK} spectrum after subtracted background. a) with M_{KK} range from 0.9 to 1.6 GeV. b) fitting of M_{KK} at M_ϕ range.

through the resonant channels

$$D^+ \to (K\pi)(K\pi), \ (KK)(\pi\pi), \ (KK\pi)(\pi), \ (K\pi\pi)(K) \qquad (4.6)$$

These are many more amplitudes than the sister analysis, $D^0 \to K^+K^-\pi^+\pi^-$ recently published by CLEO [29], and they are listed in Table [?] (which does not include possible non-resonant components not partial waves). The reason is the presence of the π^0 in our final state, which can resonate with all the other particles. There are also more 3-body resonances which can include a π^0, compared to the all charged final state. Finally, in this analysis the signal to background ratio is about 0.78, whereas in Ref. [29] it is about 17.5 for CLEO-c data.

Table 4.1: List of intermediate resonances in the decay $D^+ \to K^+K^-\pi^+\pi^0$.

(KK)	$(\pi\pi)$	$(KK\pi)$	$(K\pi)$	$(K\pi\pi)$
$\phi(1020)$	$\rho(770)$	$b_1(1235)$	$K^*(890)$	$K_1(1270)$
$f_2(1270)$	$f_0(980)$	$a_1(1260)$	$K^*(1410)$	$K_1(1400)$
$a_2(1320)$	-	$f_1(1285)$	$K_2^*(1430)$	$K_2^*(1430)$
$f_2'(1525)$	-	$\eta(1405)$	$K^*(1680)$	$K^*(1680)$
-	-	$f_1(1420)$	-	-
-	-	$a_0(1450)$	-	-
-	-	$\eta(1475)$	-	-
-	-	$\eta_2'(1645)$	-	-
-	-	$\phi(1680)$	-	-
-	-	$\rho_3(1690)$	-	-

Fig. 4.3 shows the quasi-Dalitz plot of $\phi\pi\pi^0$ in M_{bc} signal region and background region, defined as the side-band $1.84GeV < M_{BC} < 1.86GeV$. The chosen axes of the Dalitz plot are the $(\phi\pi^+)$ squared invariant mass, $y = M_{\phi\pi^+}^2$ and the $(\pi^+\pi^0)$ squared invariant mass, $x = M_{\pi^+\pi^0}^2$.

The fit is performed with an unbinned likelihood technique. To constrain the background parameters, the background distribution is fitted first, with a complete
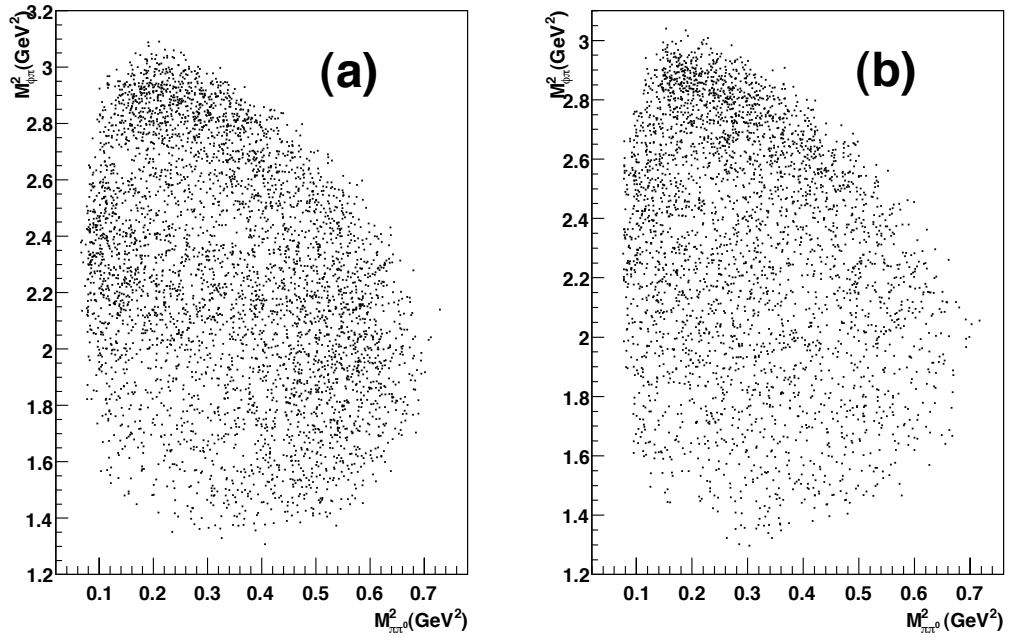
Figure 4.3: Dalitz plot for $\phi\pi\pi^0$ with x axis $M^2_{\pi^+\pi^0}$ and y axis $M^2_{\phi\pi^+}$ in (a) M_{bc} signal region and (b) in M_{bc} background region.

third order polynomial (10 free parameters). The unbinned likelihood is

$$L(x, y; \alpha) = \Pi_i P_i(x_i, y_i; \alpha) \tag{4.7}$$

with

$$P_i(x_i, y_i; \alpha) = K(\Sigma a_{ij} x^i y^j), \quad i + j < 4, \tag{4.8}$$

and K is a normalization constant. To improve the chances of a proper convergence, the starting value of the fit algorithm are calculated so as to match exactly the first 10 moments of the experimental background distribution. This gives the first background function $B_1(x, y)$.

A second, minor source of background is obtained from events which are true D^+ events, but the (KK) pair is not resonant. They are obtained from the sideband $1.04 < M_{KK} < 1.30$ GeV, and this background is treated equivalently. This gives the second background function $B_2(x, y)$. The normalizations of these two backgrounds is calculated directly from the fits previously performed.

The signal part of the fit can be determined as follows. For true ϕ, there are no known resonances that decay to $\phi\pi^+$ or $\phi\pi^0$, although numerous upper limits exist [11]. The signal part of the fit will simply include a phase space term, a $\rho^+ \rightarrow \pi^+\pi^0$ term, and their interference. The total fitting function is still the unbinned likelihood, using as probability density

$$P(x, y) = \frac{N_1 K_1 B_1(x, y) + N_2 K_2 B_2(x, y) + N(A_\rho K_3 BW(x; M_\rho, \Gamma_\rho) + A_{PS} K_4 e^{i\theta})^2)}{N_{tot}}, \tag{4.9}$$

where the K_i quantities are calculable normalization factors. The results yield $\cos\theta = (0.020 \pm 0.009)$. It is noted that the interference term is small, so that a branching fraction $D^+ \rightarrow \phi\rho^+$ can be quoted directly.
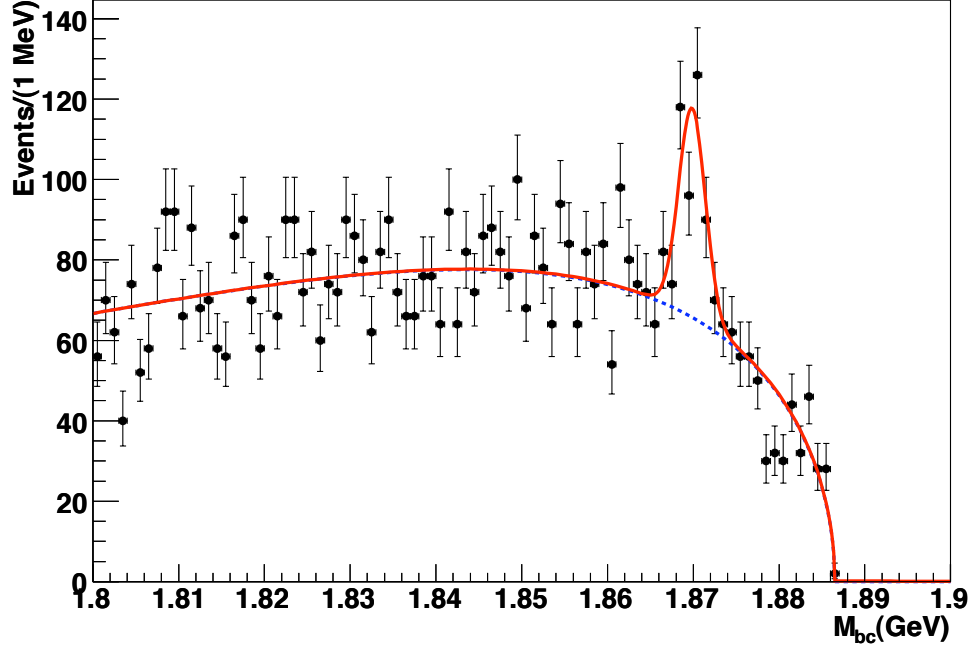
Figure 4.4: Single tag M_{bc} distribution of the $D^+ \to K^+K^-K^+$ sample.

4.1.4 Selection of $D^+ \to K^+K^-K^+$

We also applied similar technique to select the final state $K^+K^-K^+$. The binned likelihood fitting was applied to the M_{bc} spectrum, with the fitting function formed of a core gaussian signal with Argus background function. The fitting results are shown in Fig. 4.4 The fitting yields 200 ± 29 signal candidates with corresponding χ^2/dof equal to 1.514 (146/97).

4.1.5 Selection of $D^+ \to K^+K^-\pi^+\pi^-\pi^+$

Another final state that we studied was $D^+ \to K^+K^-\pi^+\pi^-\pi^+$. The M_{bc} spectrum with a core gaussian signal plus Argus background function. The fitting yields
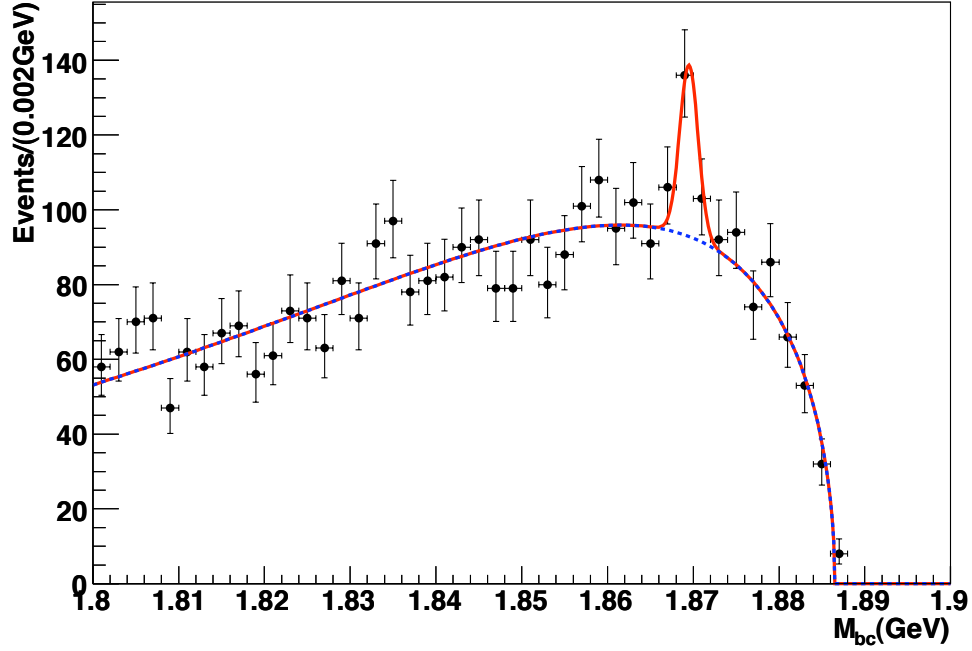
Figure 4.5: Single tag M_{bc} distribution for $D^+ \rightarrow K^+K^-\pi^+\pi^-\pi^+$.

(62 ± 27) signal events, with corresponding χ^2/dof equal to 0.849 (39.9/47).

The fitting of all modes are summarized in Table 4.2.

4.2 Efficiencies, cross checks, systematic errors and final results.

In this section, the method of getting efficiencies, detailed calculations and systematic errors analysis will be presented.

4.2.1 Efficiencies

Efficiencies are computed starting with signal MC which were in all cases generated according to phase space distributions. The efficiencies as calculated from phase space

Table 4.2: Summary of fitting results for all modes.

Modes	N_{sig}	χ^2/dof
$D^+ \to K^+K^-\pi^+\pi^0$ S	5168 ± 100	$149/95$
$D^+ \to K^+K^-\pi^+\pi^0$ D	5096 ± 159	$96.3/95$
$D^+ \to \phi\pi^+\pi^0$ S	1383 ± 31	$158/94$
$D^+ \to \phi\pi^+\pi^0$ D	113 ± 20	$161/97$
$D^+ \to K^+K^-K^+$ S	200 ± 29	$146/97$
$D^+ \to K^+K^-\pi^+\pi^-\pi^+$ S	62 ± 24	$39.9/47$

signal MC are listed in Table 4.3.

Significant differences in data and signal MC were investigated by direct inspection of the plots of the five different kinematic quantities that comprise the 4-body phase space. They are the invariant masses of the two particle combinations, M_{KK} and $M_{\pi\pi}$. The next two are $\cos^2(\theta_{KK})$ and $\cos^2(\theta_{\pi\pi})$. The angle θ_{KK} is defined as the angle between the momentum of the K^+, in the (K^+K^-) rest frame, and the momentum of the D^+ candidate. The angle $\theta_{\pi\pi}$ is defined similarly. The last kinematic variable is the angle $\Delta\phi$, which is obtained by rotating the event so that the (KK) and $(\pi\pi)$ momenta are along the $z-$axis. $\Delta\phi$ is then the azimuthal difference between the (KK) and $(\pi\pi)$ decay planes.

It was found that the dominant difference between data and MC was in the variables M_{KK} and $\cos^2(\theta_{KK})$, as shown in Fig. 4.6.

The distribution differences are obvious and are quantified next. To match the experimental distributions, a slice-and-dice method is used. The phase space of the 4-body decay is divided first in 25 cells, a 5×5 in the two variables of interest. For cross checking, we also do the calculation in 625 cells, $5 \times 5 \times 5 \times 5$ slicing and dicing and four kinematic variables, excluding the variable $\Delta\phi$. This is necessary because the algorithm performs a new M_{BC} fit for each phase space cell, and the statistical limitations do not allow successful fitting of 5^5, or 3125, cells. The $\Delta\phi$ disitributions for data and MC were found to be indistinguishable, and the dependence of the
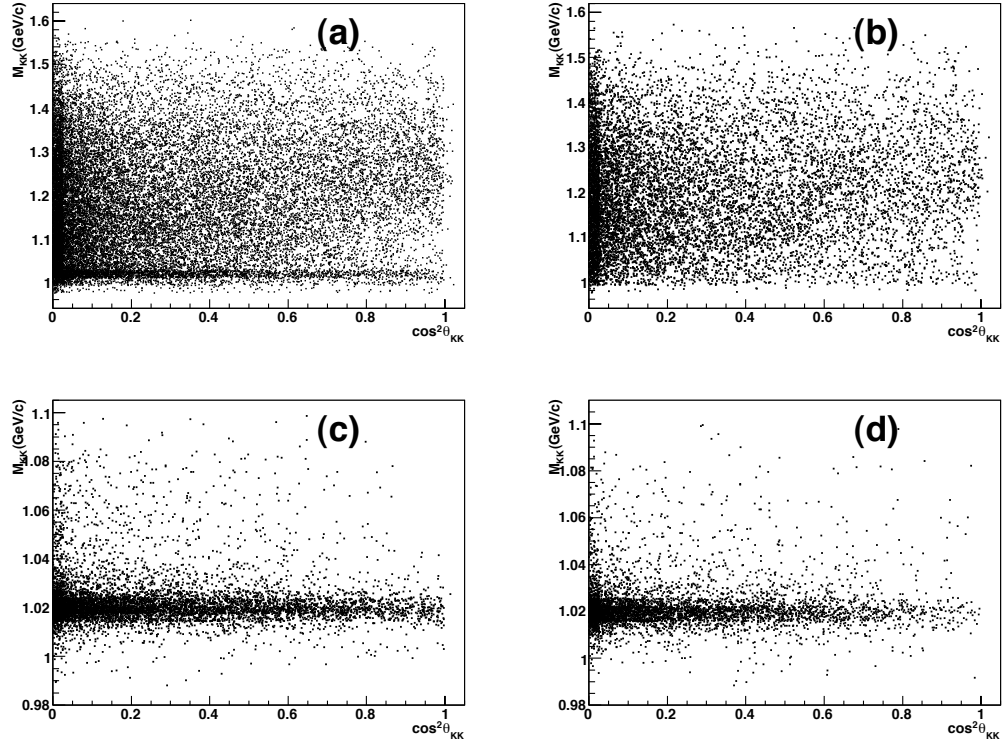
Figure 4.6: Single tag M_{KK} vs $cos^2\theta_{KK}$ plots in: a) data, b) phase space signal MC data, c) $D^+ \to \phi\pi^+\pi^0$ signal MC data, d)$D^+ \to \phi\rho^+$ signal MC data.

efficiency on $\Delta\phi$ is dropped.

The cells widths are chosen so that that the population of each cell is approximately equivalent. The efficiency is then computed by first finding the partial efficiency for each cell

$$\epsilon^i = \frac{N^i_{rec}}{N^i_{gen}},$$

where N^i_{gen} and N^i_{rec} are the generated and reconstructed MC events in cell i. Then the efficiency is

$$\epsilon = \Sigma_i \epsilon^i \frac{N^i_{sig}}{N_{sig}} \tag{4.10}$$

where N^i_{sig} is the number of fitted signal events in the data in cell i. The results are shown in Table 4.3 It is noted that just correcting for the (KK) kinematic variables M_{KK} and $\cos\theta_{KK}$ achieves satisfactory convergence of the calculation.

Table 4.3:   Efficiencies from phase space and corrections. * means the number is used in the final branching fraction calculation. ST stands for single tag, and DT for double tag.

	Efficiency (%)
$KK\pi\pi^0$ Phase Space (single tag)	24.73 ± 0.38
$KK\pi\pi^0$ ST $M_{KK}, \cos\theta_{KK}$*	16.71 ± 0.34
$KK\pi\pi^0$ ST $M_{KK}, \cos\theta_{KK}, M_{\pi\pi}, \cos\theta_{\pi\pi}$	16.62 ± 0.89
$KK\pi\pi^0$ DT $M_{KK}, \cos\theta_{KK}$*	18.32 ± 0.54
$\phi\pi\pi^0$ signal MC (single tag)	19.81 ± 0.21
$\phi\pi\pi^0$ ST $M_{KK}, \cos\theta_{KK}$*	15.62 ± 0.31
$\phi\pi\pi^0$ DT $M_{KK}, \cos\theta_{KK}$*	15.11 ± 0.57
KKK ST phase space*	34.30 ± 0.29
$KK\pi\pi\pi$ ST phase space*	24.81 ± 0.16

The results of this procedure are shown in Table 4.3, where they can be compared with the efficiency from the uncorrected phase space distributions. The results differ by less than 1% relative error. For the rare decays $D^+ \to K^+K^-\pi^+\pi^+\pi^-$ and $D^+ \to K^+K^-K^+$ the efficiency was calculated from the phase space distribution.

4.2.2 Branching fractions calculation

Since all necessary information has been collected, the branching fraction could be calculated by suing equation 3.2. The calculation are shown as followed, and in the equations, ϵ_{π^0} represents the factor of efficiency difference from data to Monte Carlo (discussed in Chapter 3) and 0.489 accounts for the branching fraction $B(\phi \to K^+ K^-)$.

- $B(D^+ \to KK\pi\pi^0)$ in single tag

$$B = \frac{N_{sig}}{\epsilon N_{DD}}\epsilon_{\pi^0} = \frac{5168}{0.167 \times 2 \times 2.354 \times 10^6} \times 1.064 \times 100\% = 0.699\% \quad (4.11)$$

- $B(D^+ \to \phi\pi\pi^0)$ in single tag.

$$B = \frac{N_{sig}}{0.489\epsilon N_{DD}}\epsilon_{\pi^0} = \frac{1383}{0.156 \times 2 \times 2.354 \times 10^6 \times 0.489} \times 1.064 \times 100\% = 0.409\%$$
$$(4.12)$$

- $B(D^+ \to K^+ K^- K^+)$ in single tag.

$$B = \frac{N_{sig}}{\epsilon N_{DD}} = \frac{200}{0.343 \times 2 \times 2.354 \times 10^6} \times 100\% = 0.01238\% \quad (4.13)$$

- $B(D^+ \to K^+ K^- \pi^+ \pi^- \pi^+)$ in single tag.

$$B = \frac{N_{sig}}{\epsilon N_{DD}} = \frac{62}{0.248 \times 2 \times 2.354 \times 10^6} \times 100\% = 0.00531\% \quad (4.14)$$

4.2.3 Cross checks.

Two significant cross checks of the analysis chain were obtained from generic MC data. The generic MC data 43,44,45 and 46 were studied, which are 18 times the statistics of the data sample. The branching fraction of $D^+ \to K^+ K^- \pi^+ \pi^0$ in generic

MC is set at 1.47%. And by using our single tag and double tag technique, our results for generic MC data is (statistical error only)

- $B(D^+ \to KK\pi\pi^0) = (1.46 \pm 0.04)\%$ in single tag,

- $B(D^+ \to KK\pi\pi^0) = (1.49 \pm 0.04)\%$ in double tag.

By a minimal modification of our software, the state $D^+ \to K^-\pi^+\pi^+$ could be selected, which has been well measured previously in CLEO to have a branching fraction of $9.14 \pm 0.10 \pm 0.16 \pm 0.07\%$ [23]. By the single tag technique, our analysis chain resulted in a branching ratio of results (9.04 ± 0.14), statistical error only, which is within 1σ error.

4.2.4 Systematic errors.

The main systematic error is from a discrepancy between data and MC π^0 reconstruction efficiency. This was measured in Ref. [30] using tagged π^0 from D decays. By selecting double tag $D^0 \to K^-\pi^+\pi^0$ decays, the π^0 could be reconstructed inclusively by requiring a missing mass consistent with the π^0 hypothesis. The method also measures the π^0 3-momentum, so that the detector and reconstruction efficiency can be mapped in data and Monte Carlo, and any discrepancy can be corrected for. This results in a linear correction to the Monte Carlo efficiency of

$$C(E) = a_0 + a_1 E(GeV),$$

with

$$a_0 = (0.939 \pm 0.022), \; a_1 = (0.001 \pm 0.021), \; \rho = -0.947.$$

Systematics from track reconstruction are 0.3% per track and added linearly [31], and systematics from efficiency calculations are assigned a 1.0% value.

Systematic errors from varying the ϕ mass and width in the fits within the errors quoted in Ref. [11] were also tested, resulting in a 0.1% systematics.

Systematics from the fitting procedure are calculated as follows:

- each nuisance free parameter in Eq.4.3 is varied by one standard deviation and kept fixed while the fit is being repeated. The results are shown in the Table 4.4 Table 4.5; Table 4.6 and Table 4.7.

- The same procedure is repeated for Eq.4.4.

- The rare decay fits $D^+ \to K^+K^-\pi^+\pi^+\pi^-$ and $D^+ \to K^+K^-K^+$ are treated similarly to $D^+ \to K^+K^-\pi^+\pi^0$.

Table 4.4: Fitting results with one fixed parameter 1σ from the fitting value in single tag in $D^+ \to K^+K^-\pi^+\pi^0$.

Fitting parameters	Fitting results	percentage difference
Double gaussian yields for signal	5055 ± 654	-2.187%
Fixed Argus with -1σ	5096 ± 159	-1.393%
Fixed Argus with +1σ	5273 ± 166	2.032%
Fixed width of one gaussian at -1σ	5048 ± 514	-2.322%
Fixed width of one gaussian at +1σ	5119 ± 489	-0.948%

Table 4.5: Fitting results with one fixed parameter 1σ from fitting value in single tag in $D^+ \to \phi\pi^+\pi^0$.

Fitting parameters	Fitting results	percentage difference
Double gaussian yields for signal	1408 ± 117	1.808%
Fixed width of gaussian at -1σ	1379 ± 56	-0.289%
Fixed width of gaussian at +1σ	1411 ± 67	2.025%

To particularly address the limitations of our Dalitz plot analysis, the ϕ fit was done with and without interference terms. The difference is assumed to be part of the systematics and it is listed.

Table 4.6: Fitting results with one fixed parameter 1σ from fitting value in single tag in $D^+ \to K^+K^-K^+$.

Fitting parameters	Fitting results	percentage difference
Fixed argus at -1σ	203 ± 29	1.500%
Fixed argus at +1σ	196 ± 28	-2.000%
Fixed width of gaussian at +1σ	209 ± 29	4.500%
Fixed width of gaussian at -1σ	195 ± 37	-2.500%

Table 4.7: Fitting results with one fixed parameter 1σ from fitting value in single tag in $D^+ \to K^+K^-\pi^+\pi^+\pi^-$.

Fitting parameters	Fitting results	percentage difference
Fixed argus at -1σ	54 ± 19	-12.90%
Fixed argus at +1σ	73 ± 24	17.74%
Fixed width of gaussian at +1σ	76 ± 20	22.58%
Fixed width of gaussian at -1σ	52 ± 15	-16.13%

The assigned systematics are listed in Table 4.8 and the final branching ratios, including systematic errors, are shown in Table 4.9. For all final results, the single tag result is chosen over the double tag result. The signal for $D^+ \to K^-K^+\pi^+\pi^-\pi^+$ is weak, only about two standard deviations, although still a world best measurement. It is quoted both as an upper limit and a central value.

4.3 Conclusions.

Table 4.9 shows the final results of this analysis.

The results of this analysis can be summarized as follows:

- the branching ratios $D^+ \to K^+K^-\pi^+\pi^0$ and $D^+ \to \phi\pi^+\pi^0$ have improved by factors of 10 over previous measurements. The results for $D^+ \to K^+K^-\pi^+\pi^+\pi^-$ and $D^+ \to K^+K^-K^+$ are comparable with current world averages in both central value and error.

- the inclusive and exclusive decay fractions of the $D^+ \to \phi X$ are now in good

Table 4.8: Summaries of non-fitting systematic errors for all decay modes in single tag measurement.

Decay mode	Sources	Systematic errors (%)
$D^+ \to K^+K^-\pi^+\pi^0$	tracks reconstruction	0.9%
	photon reconstruction	2.0%
	PDG systematic error	0.2%
	efficiency	1.0%
	DD pair number	1.0%
$D^+ \to \phi\pi^+\pi^0$	tracks reconstruction	0.9%
	photon reconstruction	2.0%
	PDG systematic error	0.3%
	efficiency	1.0%
	DD pair number	1.0%
$D^+ \to \phi\rho^+$	tracks reconstruction	0.9%
	photon reconstruction	2.0%
	PDG systematic error	0.3%
	DD pair number	1.0%
$D^+ \to K^+K^-\pi^+\pi^+\pi^-$	track reconstruction	1.5%
	PDG systematic error	0.2%
	efficiency	1.0%
	DD pair number	1.0%
$D^+ \to K^+K^-K^+$	tracks reconstruction	0.9%
	PDG systematic error	0.2%
	efficiency	1.0%
	DD pair number	1.0%

agreement. The ratio R from Eq. 1.6 is now

$$R = \frac{B(D^+ \to \phi\pi^+\pi^0) + B(D^+ \to \phi\pi^+)}{B(D^+ \to \phi X)} = 0.923 \pm 0.117.$$

The results are consistent with the two decays saturating the inclusive branching ratio.

- the decay $D^+ \to \phi\rho^+$ has been observed for the first time. This decay, too, appears to dominate the $D^+ \to \phi\pi^+\pi^0$ channel.

Table 4.9: Final results for this analysis. The first error is statistical and the second error is systematic.

Decay mode	Branching ratio (%)
$D^+ \to K^+K^-\pi^+\pi^0$	$0.699 \pm 0.021 \pm 0.005$
$D^+ \to \phi\pi^+\pi^0$	$0.409 \pm 0.012 \pm 0.006$
$D^+ \to \phi\rho^+$	$0.313 \pm 0.053 \pm 0.014$
$D^+ \to \phi\pi^+ + D^+ \to \phi\pi^+\pi^0$	0.951 ± 0.036
$D^+ \to K^+K^-\pi^+\pi^+\pi^-$	$0.00531 \pm 0.00206 \pm 0.0005$
$D^+ \to K^+K^-K^+$	$0.01238 \pm 0.00180 \pm 0.0008$

REFERENCES

[1] N. Cabibbo, *Physical Review Letters* 10 (12): 531533 1963

[2] S. L. Glashow, *Nucl. Phys.* 22:579, 1961

[3] S. Weinberg, *Phys. Rev. Lett.* , 19: 1264, 1967

[4] A. Salam, *Elementary Particle Theory*, N. Svartholm, ed., Stockholm: Almguist and Wiksell, 1968

[5] D.J. Gross, F.Wilczek, *Phys. Rev. Lett*, 30:1343, 1973

[6] H.D. Politzer, *Phys. Rev. Lett*, 30:1346 1973

[7] M.L. Perl *et al*, *Physics Review Letters*, 35(22):1489, 1975

[8] E. Noether, *Math. Phys.*, 235-257, 1918

[9] T. D. Lee and C.N. Yang, *Phys. Rev.* , 104:254-258, 1956

[10] C.S. Wu, E. Ambler, R.W. Hayward, D.D. Hoppes and Hudson, *Phys. Rev.* 105:4, 1957

[11] K. Nakamura *et al.*, *Journal of Physics*, **37**(75021):150, 2010

[12] J.Iliopoulos, L.Maiani, S.L. Glashow, *Phys. Rev. D*, 2:1285, 1970

[13] M. Kobayashi and T. Maskawa, *Progr. Theor. Phys.*, 49: 652-657, 1973

[14] J.E. Augustin *et al.*, *Physical Review Letters*, 33(23): 1406, 1974

[15] J.J.Aubert *et al.*, *Physical Review Letters*, 33(23): 1404, 1974

[16] B. Bhattacharya, J. L. Rosner, *Phys. Rev. D* 77, 114020, 2008

[17] P. Bedaque, A.Das, V.S.Mathur, *Physical Review*, **49**, 1, 1994

[18] Harry J. Lipkin, *Physics Letters B*, 515 81-88, 2001

[19] R. A. Briere *et al*, *CLNS*, CLEO-c and CESR-c: A New Frontier of Weak and Strong Interactions, 1/1742, 2010

[20] CESR and CLEO staff, *CLNS 93/1265*, Laboratory for Elementary-Particle Physics, Publication (1993)

[21] Cerenkov, P.A. *Physical Review*, **52**:378, 1937

[22] M.Artuso *et al.* CBX05-36

[23] X.Shi, P.Onyisi, J.Alexander, D.Cassel, A.Cassel. CBX 2011-003

[24] S. Stroinev, A.Ryd, W.Sun,P.Onyisi,D.Cassel, CBX 2008-040

[25] L.Fields, R.Patterson, CBX 2008-029

[26] S.Stroiney, W.Sun, CBX 2006-11

[27] H.Albrecht, *Physics Letters B* textbf340(3):217-220, 1994

[28] M. J. Oreglia, Ph.D Thesis, SLAC-236 (1980), J. E. Gaiser, Ph.D. Thesis, SLAC-255 (1982).

[29] M. Artuso et al., CLEO Collaboration, arXiv:1201.5716

[30] L. Fields and R. Patterson, `CBX 2008-029`.

[31] Xin, B. and Shipsey, I., CBX 2008-027.

ABSTRACT

MEASUREMENT OF HADRONIC
$D^+ \to K^+K^-X$ **BRANCHING FRACTIONS**

by

PENG ZHOU

May 2010

Advisor: Dr. Giovanni Bonvinici

Major: Physics

Degree: Doctor of Philosophy

Using $818 pb^{-1}$ of CLEO-c data at $\sqrt{s}$ =3770 MeV, we measure precisely the branching ratios for four $D^+ \to K^+K^-X$ hadronic channels. Our measurement improves the errors of both B($D^+ \to K^+K^-\pi^+\pi^0$) and B($D^+ \to \phi\pi^+\pi^0$) by a factor of 10. We report first observation of the decay $D^+ \to \phi\rho^+$, as well as branching ratio measurements for two rare decays.

AUTOBIOGRAPHICAL STATEMENT

Name: Peng Zhou

I was born in Lanzhou, Gansu, China on Jan 16th, 1983 and started my undergraduate in **University of Science and Technology of China** in 2002. In 2006, I received my Bachelor of Science degree in physics. Since 2007, I became a graduate student in Department of Physics in **Wayne State University** and then in summer 2008, I firstly start my graduate research in CLEO with Prof. Bonvicini.